

Resolved galactic superwinds reconstructed around their host galaxies at $z > 3$

Mandy C. Chen^{1*}, Hsiao-Wen Chen¹, Max Gronke^{2†}, Michael Rauch³, and Tom Broadhurst^{4,5,6}

¹*Department of Astronomy and Astrophysics, The University of Chicago, Chicago, IL 60637, USA*

²*Department of Physics & Astronomy, Johns Hopkins University, Baltimore, MD 21218, USA*

³*Carnegie Observatories, 813 Santa Barbara Street, Pasadena, CA 91101, USA*

⁴*Department of Theoretical Physics, University of the Basque Country UPV/EHU, Bilbao, Spain*

⁵*Donostia International Physics Center (DIPC), 20018 Donostia, Spain*

⁶*IKERBASQUE, Basque Foundation for Science, Bilbao, Spain*

Accepted XXX. Received YYY; in original form ZZZ

ABSTRACT

This paper presents a detailed analysis of two giant Lyman-alpha ($\text{Ly}\alpha$) arcs detected near galaxies at $z = 3.038$ and $z = 3.754$ lensed by the massive cluster MACS 1206–0847 ($z = 0.44$). The $\text{Ly}\alpha$ nebulae revealed in deep MUSE observations exhibit a double-peak profile with a dominant red peak, indicating expansion/outflowing motions. One of the arcs stretches over $1'$ around the cluster Einstein radius, resolving the velocity field of the line-emitting gas on kpc scales around three star-forming galaxies of $0.3\text{--}1.6 L_*$ at $z = 3.038$. The second arc spans $15''$ in size, roughly centered around two low-mass $\text{Ly}\alpha$ emitters of $\approx 0.03 L_*$ at $z = 3.754$. All three galaxies in the $z = 3.038$ group exhibit prominent damped $\text{Ly}\alpha$ absorption (DLA) and several metal absorption lines, in addition to nebular emission lines such as $\text{He II}\lambda 1640$ and $\text{C III}\lambda\lambda 1906, 1908$. Extended $\text{Ly}\alpha$ emission appears to emerge from star-forming regions with suppressed surface brightness at the center of each galaxy. Significant spatial variations in the $\text{Ly}\alpha$ line profile are observed which, when unaccounted for in the integrated line, leads to biased constraints for the underlying gas kinematics. The observed spatial variations indicate the presence of a steep velocity gradient in a continuous flow of high column density gas from star-forming regions into a low-density halo environment. A detailed inspection of available galaxy spectra shows no evidence of AGN activity in the galaxies, and the observed $\text{Ly}\alpha$ signals are primarily explained by resonant scattering. The study presented in this paper shows that spatially-resolved imaging spectroscopy provides the most detailed insights yet into the kinematics of galactic superwinds associated with star-forming galaxies.

Key words: galaxies: kinematics and dynamics – galaxies:ISM – intergalactic medium – galaxies: high-redshift – galaxies: evolution

1 INTRODUCTION

The formation and evolution of galaxies are intimately connected to the properties of the circumgalactic medium (CGM). Characterizing the interactions between galaxies and their surrounding gas, such as gas infall and outflows, is a critical step toward improving our still patchy understanding of the life cycles of baryons and galaxy evolution over cosmic time. But because of the low-density nature of the CGM, studying such tenuous gas has historically relied on absorp-

tion spectroscopy along individual QSO sightlines. Over the past few decades, absorption-line studies have yielded sensitive, mostly one-dimensional constraints on the gas density, temperature, metallicity and kinematics in the circumgalactic space (see the review by [Chen 2017](#); [Tumlinson et al. 2017](#); [Rudie et al. 2019](#), and references therein). However, uncertainties remain in connecting gas to galaxies in the absence of a spatially-resolved two-dimensional map of the gas. To access the spatial information of gas distribution in the CGM, direct detections of the tenuous gas in emission provide a promising avenue. The hydrogen $\text{Ly}\alpha$ line, being the strongest emission line expected of photo-ionized gas at a temperature $T \sim 10,000$ K, provides a sensitive probe of

* E-mail: mandychen@astro.uchicago.edu

† Hubble Fellow

the tenuous CGM (e.g., [Osterbrock & Ferland 2006](#); [Draine 2011](#)). At $z \approx 2-7$, the Ly α line at 1215 Å is conveniently redshifted into the atmospheric transmission window and becomes accessible on the ground. In the past two decades, narrow-band imaging and deep long-slit spectroscopic observations have successfully revealed extended line-emitting gas around galaxies (e.g., [Adelberger et al. 2006](#); [Rauch et al. 2008, 2011](#); [Steidel et al. 2011](#); [Xue et al. 2017](#)) and QSOs (e.g., [Hennawi et al. 2009](#); [Cantalupo et al. 2012, 2014](#)). Those observations have shed light on several important physical processes in the CGM, such as the ubiquity of large-scale gas flows on 10–100 physical kpc (pkpc) scales at high redshifts (e.g., [Rauch et al. 2016](#)) and the non-trivial contribution of star-forming galaxies to reionization (e.g., [Dijkstra 2014](#); [Matthee et al. 2018](#)).

The recent advent of high-throughput, wide-field optical integral field spectrographs (IFSs) on large ground-based telescopes, such as the Multi Unit Spectroscopic Explorer (MUSE) on the Very Large Telescopes (VLT) ([Bacon et al. 2010](#)) and the Keck Cosmic Web Imager (KCWI) on the Keck Telescopes ([Morrissey et al. 2018](#)) has brought a significant breakthrough in systematically uncovering extended Ly α emission in typical, low-mass galaxies as well as QSOs at $z \approx 2-7$ (e.g., [Wisotzki et al. 2016, 2018](#); [Borisova et al. 2016](#); [Leclercq et al. 2017](#); [Cai et al. 2017, 2019](#); [Arrigoni Battaia et al. 2019](#)). These sensitive IFS observations have uncovered extended Ly α emission out to > 20 times the spatial extent of the stellar continuum, and revealed key insights into the physical nature of these extended Ly α sources. For example, significant spatial variations of Ly α line profiles are directly observed within a single line-emitting nebula (e.g., [Rauch et al. 2013](#); [Vanzella et al. 2017](#); [Erb et al. 2018](#)). In addition, there exists a positive correlation between the full-width-at-half-maximum (FWHM) of the Ly α line and the continuum UV brightness of the associated star-forming galaxies (e.g., [Wisotzki et al. 2018](#); [Leclercq et al. 2020](#)), indicating an intimate connection between the origin of the Ly α photons and star-forming activities (e.g., [Dijkstra & Kramer 2012](#); [Cantalupo 2017](#)).

Multiple processes can lead to Ly α emission in the CGM, such as fluorescence powered by ionizing photons from star-forming regions or active galactic nuclei (AGN), cooling radiation, and scattering of Ly α photons by mostly neutral hydrogen gas (e.g., [Hogan & Weymann 1987](#); [Gould & Weinberg 1996](#); [Cantalupo et al. 2005](#); [Kollmeier et al. 2010](#); [Faucher-Giguère et al. 2010](#); [Hennawi & Prochaska 2013](#)). Disentangling different processes that contribute to the observed Ly α signal is challenging due to the resonant scattering nature of Ly α photons, especially when Ly α is the only observable line feature from the emission regions. At the same time, the detailed double-peak profiles of spectrally-resolved Ly α lines provide a sensitive probe of the underlying gas kinematics. It is expected that Ly α emission originating in infalling and outflowing medium will result in blue-enhanced and red-enhanced peak, respectively (e.g., [Dijkstra 2017](#), and references therein). This has motivated increasingly sophisticated Monte Carlo radiative transfer models that incorporate different gas geometry and kinematics to accurately track Ly α photon scattering and infer the physical properties of the gaseous clouds (e.g., [Dijkstra et al. 2006](#); [Verhamme et al. 2006](#); [Hansen & Oh 2006](#); [Laursen et al. 2009](#); [Schaerer et al. 2011](#); [Gronke et al. 2015](#)).

These Monte Carlo Ly α radiative transfer codes can generally reproduce the observed Ly α line width based on a combination of thermal broadening and bulk motions, but significant discrepancies are also seen between observations and model predictions ([Verhamme et al. 2008](#); [Kulas et al. 2012](#); [Orlitová et al. 2018](#)). Such discrepancies have both theoretical and observational implications. Theoretically, there is a lot of room for better capturing the physical processes in radiative transfer simulations, such as a realistic treatment of dust attenuation and gas clumpiness (e.g., [Laursen et al. 2009](#); [Dijkstra & Kramer 2012](#); [Gronke et al. 2016](#)). Observationally, as Ly α photons are scattered both in spectral and spatial dimensions, it is critical to obtain observations with not only high spectral resolution, but also high spatial resolution to provide the best constraints on the source environment.

Strong gravitational lensing provides sharpened images of the high-redshift Universe via an enhanced spatial resolution of highly magnified images of distant galaxies (e.g., [Coe et al. 2013](#)) and recently individual, luminous high redshift stars ([Kelly et al. 2018](#)). Massive galaxy and cluster lenses have revealed detailed properties of lensed background sources down to sub-kpc or even as detailed as tens of pc scales (e.g., [Livermore et al. 2012](#); [Bordoloi et al. 2016](#); [Johnson et al. 2017](#); [Berg et al. 2018](#); [Florian et al. 2020](#)). Multiply-lensed QSOs and extended, lensed arcs of bright background sources have been used to spatially resolve the diffuse CGM in absorption spectroscopy ([Rauch et al. 2002](#); [Chen et al. 2014](#); [Zahedy et al. 2016](#); [Rubin et al. 2018](#); [Lopez et al. 2018](#); [Mortensen et al. 2020](#)). Several gravitationally-lensed Ly α emitting nebulae have also been reported, in which the enhanced spatial resolution has aided to reveal the underlying physical environment of the source in greater details ([Swinbank et al. 2007](#); [Patrício et al. 2016](#); [Caminha et al. 2017](#); [Claeyssens et al. 2019](#); [Erb et al. 2019](#)).

Here we present a detailed analysis of two gravitationally-lensed Ly α emitting nebulae, System *A* at $z = 3.038$ (Figure 1) and System *B* at $z = 3.754$ (Figure 2), detected in deep MUSE observations of the field around the strong lensing cluster, MACS1206–0847 at $z = 0.44$ (hereafter MACS1206). Both nebulae are multiply-lensed to form giant tangential arcs in the image plane around the Einstein radius of the foreground cluster, and both exhibit a double-peaked Ly α profile. In particular, the serendipitous alignment of the nebula in System *A* results in an extended low surface brightness arc of $\text{SB}_{\text{Ly}\alpha} \approx 3 \times 10^{-18} \text{ erg s}^{-1} \text{ cm}^{-2} \text{ arcsec}^{-2}$ and $\approx 1'$ in length, comprising three contiguous lensed images ([Caminha et al. 2017](#)), while System *B* forms an arc of $\approx 15''$ in length with high surface brightness peaks exceeding $\text{SB}_{\text{Ly}\alpha} \approx 2 \times 10^{-17} \text{ erg s}^{-1} \text{ cm}^{-2} \text{ arcsec}^{-2}$. In addition, the Ly α emitting region in System *A* consists of two separate nebulae, detached from a group of three continuum sources with one being an $\approx 1.6 L_*$ galaxy and the other two being sub- L_* galaxies. All three of these galaxies exhibit prominent interstellar absorption lines, including hydrogen damped Ly α absorption (DLA) in their spectra. One of the sub- L_* galaxies (*A3* in Figure 1 below) is further resolved into two high-intensity peaks. In contrast, the Ly α nebula in System *B* exhibits a symmetric morphology in the source plane, centered approximately at two compact continuum sources separated by $\approx 0''.1$ ($\approx 0''.3-0''.5$ in the image

plane), both of which are low-luminosity $\approx 0.03 L_*$ Ly α emitters (LAE) with a rest-frame Ly α equivalent width of $W(\text{Ly}\alpha) \approx 30 \text{ \AA}$.

In this study, we examine the underlying gas flows by combining spatially-resolved Ly α emission profiles from MUSE and known star formation properties of the neighboring galaxies from available *Hubble Space Telescope* (*HST*) broadband photometry. This paper is organized as follows. First, the archival data included in our analysis are presented in Section 2, including broadband imaging data by *HST* and IFS data by VLT/MUSE. The lens models fine-tuned to best reproduce multiple images from Systems *A* and *B* are presented in Section 3. In Sections 4 and 5, we present detailed analysis of UV continuum galaxies and the Ly α line-emitting gas, respectively. We discuss our results in Section 6, and conclude in Section 7. Throughout this paper, we adopt a Hubble constant of $H_0 = 70 \text{ km/s/Mpc}$, $\Omega_M = 0.3$ and $\Omega_\Lambda = 0.7$ when deriving distances, masses and luminosities. All magnitudes quoted are in the AB system.

2 OBSERVATIONAL DATA

MACS 1206 is a well studied cluster, which was first identified as a luminous X-ray source in the ROSAT All Sky Survey (Voges et al. 1999; Böhringer et al. 2001) and later confirmed to be a massive, strong-lensing cluster by the Massive Cluster Survey (Ebeling et al. 2001, 2009). It was also selected as one of the 25 clusters in the *Cluster Lensing And Supernova Survey with Hubble* (CLASH) program (Postman et al. 2012). Exquisite imaging and spectroscopic data of this cluster field are available in public data archives, including high-quality multi-band imaging data from the *HST*, follow-up galaxy spectroscopic survey data from the CLASH-VLT redshift survey (Biviano et al. 2013; Rosati et al. 2014), and wide-field IFS data obtained using VLT/MUSE (Bacon et al. 2010; Caminha et al. 2017). High-level science products are retrieved from these public data archives for our study. In this section, we provide a summary of these data products.

2.1 *HST* images

High spatial resolution, UV, optical and near-infrared imaging data of the field around MACS 1206 obtained using the *HST* were retrieved from the Mikulski Archive for Space Telescopes (MAST) archive¹ (PI: M. Postman). These include images taken using the Advanced Camera for Surveys (ACS), the Wide Field Camera 3 (WFC3), and a suite of UV, optical, and near-infrared filters (see Table 2 below). Figures 1 and 2 show composite images of the central region of MACS 1206 from combining F475W (blue), F814W (green), and F160W (red) images, highlighting the lensing configurations of System *A* and System *B*, respectively. Detailed photometric properties of each system derived from these *HST* data are described in §4.

Given the close proximity of *B1* and *B2* in the source plane (see §5.1 below), it is possible that they correspond to distinct star-forming regions in the same galaxy at $z =$

3.754. However, without high-resolution infrared data, we cannot determine confidently whether or not *B1* and *B2* originate in the same galaxy. We therefore proceed with referring to *B1* and *B2* as individual galaxies for simplicity.

2.2 MUSE IFS Data

Wide-field IFS data of MACS 1206 were obtained using MUSE on the VLT UT4. The observations were carried out under Program ID's 095.A-0181(A) and 097.A-0269(A) to cover an effective area of 2.63 arcmin^2 around the cluster in three pointings (PI: J. Richard), which are part of a systematic survey of 12 strong lensing clusters using MUSE (Richard et al. 2020). In the region where lensed images of Systems *A* and *B* are found, a total exposure time of ≈ 4 hours were collected. Pipeline-processed and flux-calibrated data cubes were retrieved from the ESO Phase 3 Archive, covering a wavelength range of $4750\text{-}9300 \text{ \AA}$ with a spectral resolution of $\text{FWHM} \approx 170 (110) \text{ km s}^{-1}$ at $\approx 5000 (7000) \text{ \AA}$ and a pixel scale of $0''.2 \times 0''.2$. The mean point spread function (PSF) in the final combined data cube was determined using a bright star, and found to be $\approx 1''$ at 7000 \AA . Astrometry of the combined MUSE data cube was re-calibrated to match the world coordinate system of available *HST* images. The pipeline generated combined data cube contains non-negligible sky residuals that affected the detection of faint emission features. Additional sky subtraction was therefore performed using a median sky residual spectrum generated from object-free spaxels in the data cube. Detailed spectroscopic properties of both continuum sources and Ly α emitting nebulae are described in §4 and §5, respectively. Finally, the wavelength array is converted to vacuum to facilitate accurate velocity calculations based on known rest-frame UV wavelengths.

3 CLUSTER LENS MODELING

To determine the intrinsic properties of both Systems *A* and *B*, it is necessary to construct a cluster lens model to correct for the gravitational lensing effect. Here we employ the software *LENSTOOL* (version 6.5) (Jullo et al. 2007) to construct a parametric cluster lens model of MACS 1206 by incorporating known multiply-lensed galaxies identified in the MUSE data (Caminha et al. 2017) and those reported in the literature (e.g., Zitrin et al. 2012; Umetsu et al. 2012; Eichner et al. 2013). As both Systems *A* and *B* are in the core region of the cluster, we only include the strong lensing constraints and do not consider weak lensing effect in our lens modeling process. We first obtain a fiducial cluster lens model that gives a good fit to a total of 72 multiple images from 21 background sources. Those images cover a field of view (FOV) of $\approx 2'$ relatively evenly, providing robust constraints for the projected cluster mass distribution within this FOV. We then fine-tune the lens model by considering only multiple images of Systems *A* and *B*, optimising the mass distribution projected close to those particular images as well as the multiply-lensed extended Ly α emitting nebulae. Details regarding the lens modeling process are described below.

¹ https://archive.stsci.edu/pub/hlsp/clash/macs1206/data/hst/scale_30mas

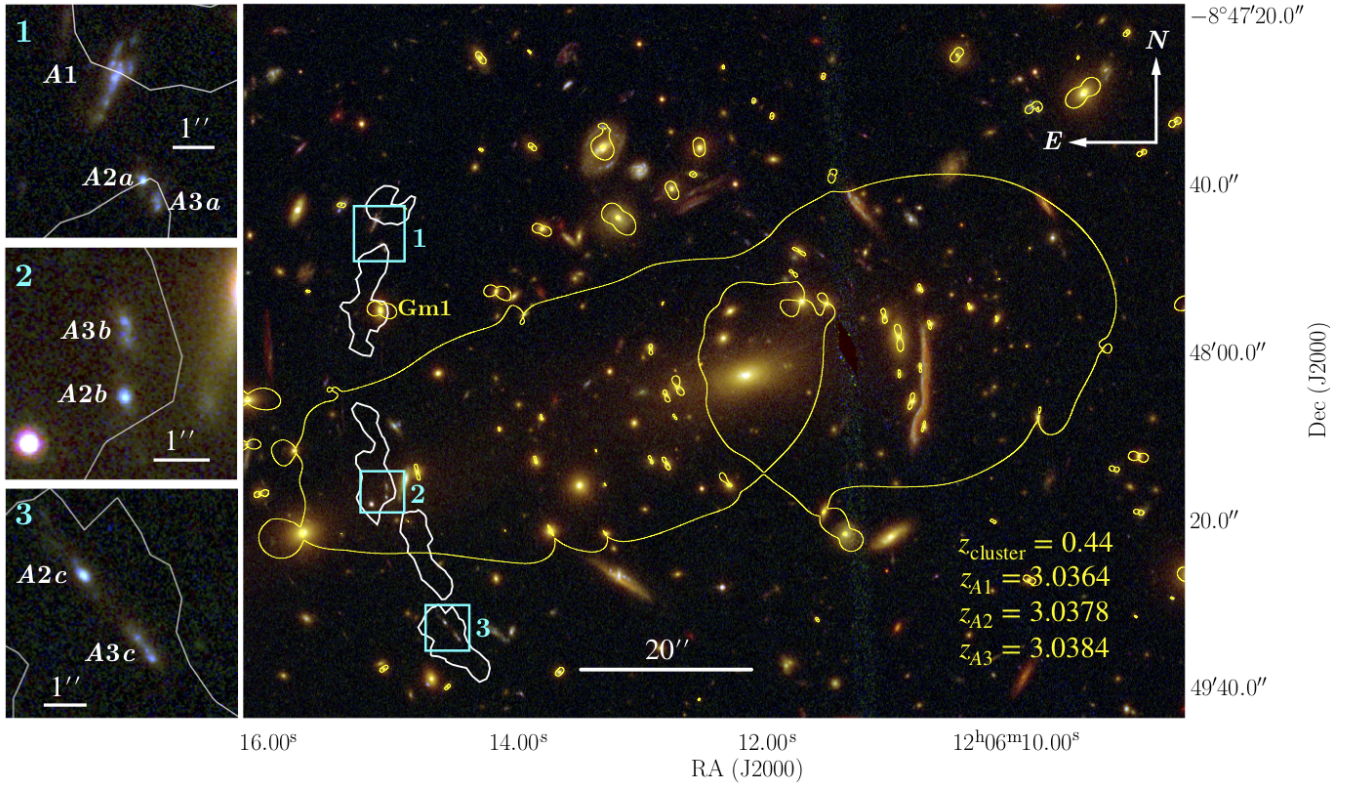


Figure 1. Composite image of the core region of MACS 1206, produced using *HST* F475W (blue), F814W (green) and F160W (red) images. White contours indicate the Ly α emission associated with System A at a surface brightness of $SB_{\text{Ly}\alpha} = 3.7 \times 10^{-18} \text{ erg s}^{-1} \text{ cm}^{-2} \text{ arcsec}^{-2}$, integrated over the spectral window of 4890–4930 Å (see § 5.1 below). The surface brightness limit corresponds to a 3- σ limiting flux over a circular aperture of 1'' in diameter, roughly the size of the PSF measured in the MUSE data. Yellow contours show the critical curve of the cluster lens for a source at $z = 3.038$. Left panels show zoomed-in regions around lensed images of galaxies A1, A2, and A3, along with the Ly α contours. Note that the galaxy A1 at $z = 3.0364$ is magnified but not multiply-lensed. Cluster member galaxy Gm1 is located close to lensed images of System A and is individually optimised in the lens modeling process as described in § 3. After correcting for the lensing magnification, the total Ly α luminosity from the nebula is $L_{\text{Ly}\alpha} = (5.2 \pm 0.1) \times 10^{42} \text{ erg s}^{-1}$ (see § 5.1).

3.1 Fiducial cluster lens model

Following Caminha et al. (2017), we adopt a parametric model based on a pseudo-isothermal elliptical mass distribution (PIEMD) (Kassiola & Kovner 1993) of ellipticity ϵ and include two additional isothermal halo components to represent the cluster-scale diffuse mass. This three-halo configuration is found to minimize the dispersion between predicted and observed image positions for all multiply-lensed sources (see Caminha et al. 2017, for detailed discussions). The convergence of PIEMD is given by

$$\kappa_c = \frac{\sigma_v^2}{2G\Sigma_{cr}\sqrt{R_\epsilon^2 + r_c^2}}, \quad (1)$$

where R_ϵ is the distance from the center of the cluster, defined as

$$R_\epsilon^2 = \frac{x^2}{(1+\epsilon)^2} + \frac{y^2}{(1-\epsilon)^2}, \quad (2)$$

r_c is the core radius and Σ_{cr} is the projected critical mass density. Given the angular diameter distances between the observer and the lens (D_l), the lens and the source (D_{ls}), and the observer and the source (D_s), the projected critical mass density is defined as

$$\Sigma_{cr} = \frac{c^2}{4\pi G} \frac{D_s}{D_l D_{ls}}. \quad (3)$$

All six parameters of the three PIEMD halos (x , y , r_c , ϵ , position angle, velocity dispersion σ_v) are free to vary. We also include external shear (parameterized by the intensity γ_{shear} and position angle θ_{shear}) to account for possible massive structures in regions further away from the cluster core.

In addition to the cluster-scale diffuse mass distribution, we account for local perturbations in the vicinity of individual galaxies by including 128 cluster member galaxies in the lens model. These member galaxies are selected based on their redshifts in the catalog of Molino et al. (2017), which is downloaded from the MAST archive². We first eliminate galaxies fainter than $AB = 24$ mag in the F160W band. For galaxies with spectroscopic redshifts, we select those with $0.425 < z_{\text{spec}} < 0.453$. For galaxies without z_{spec} , we apply the same criterion based on available photometric redshifts. A total of 128 cluster members are selected from this exercise. Note that in general, the cluster lensing potential is dominated by the large-scale diffuse mass distribution, which is primarily in the form of dark matter. Member galaxies only introduce perturbations local to the location of individual galaxies. Therefore, in cases where lensed images do

² <https://archive.stsci.edu/pub/hlsp/clash/mac1206/catalogs/molino/>

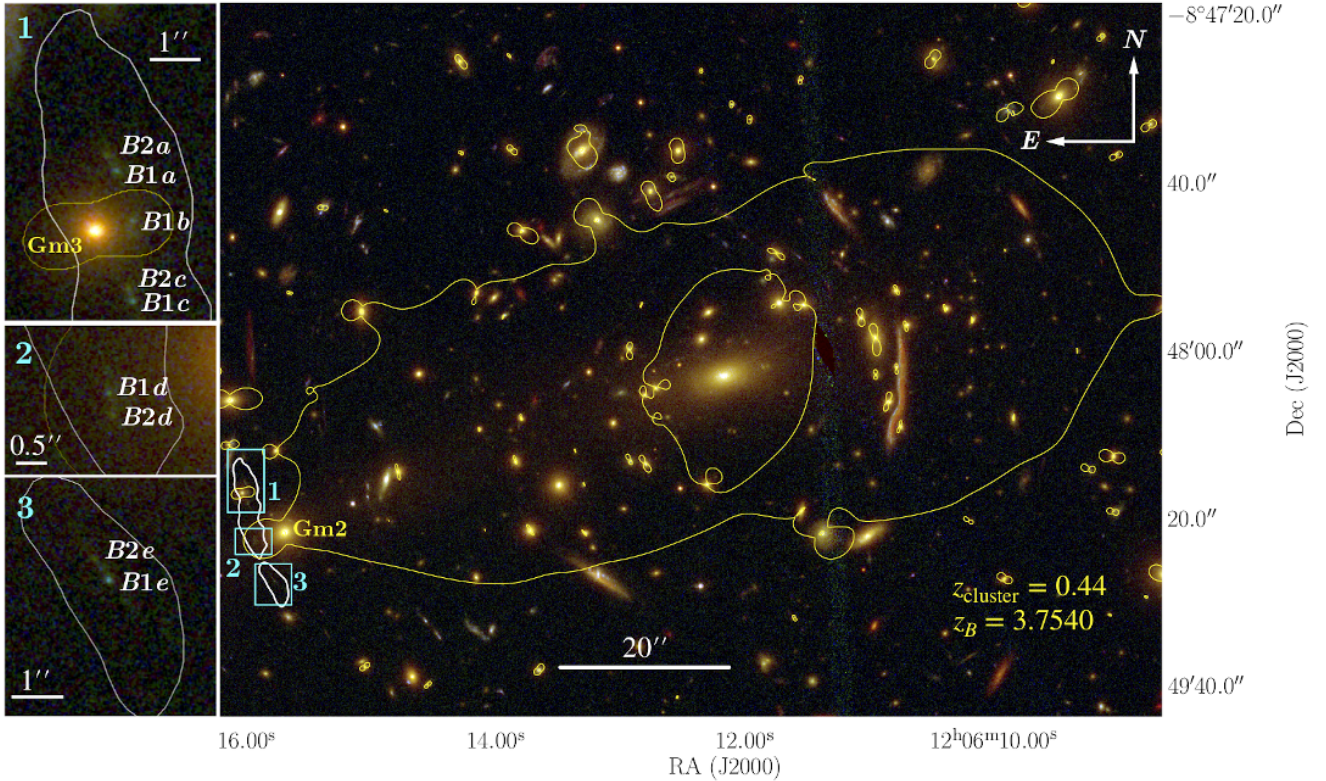


Figure 2. Same as Figure 1, while highlighting the configuration of System *B*. White contours indicate the Ly α emission associated with System *B* at $SB_{\text{Ly}\alpha} = 2.8 \times 10^{-18} \text{ erg s}^{-1} \text{ cm}^{-2} \text{ arcsec}^{-2}$, integrated over the spectral window of 5766–5796 Å (see § 5.1 below). The surface brightness limit corresponds to a $3\text{-}\sigma$ limiting flux over a circular aperture of $1''$ in diameter, roughly the size of the PSF measured in the MUSE data. Yellow contours show the critical curve of the cluster lens for a source at $z = 3.754$. Left panels show zoomed-in regions around the lensed images of galaxy *B* consisting of components *B1* and *B2*, along with the Ly α contours. Cluster member galaxies Gm2 and Gm3 are located close to lensed images of System *B* and are individually optimised in the lens modeling process as described in §3. After correcting for the lensing magnification, the total Ly α luminosity from the nebula is $L_{\text{Ly}\alpha} = (9.8 \pm 0.2) \times 10^{41} \text{ erg s}^{-1}$ (see §5.1).

not appear close to individual member galaxies ($\leq 5''$, corresponding to typical Einstein radius of individual galaxies), the variation in the selection of member galaxies does not introduce significant uncertainties to the cluster lensing potential. However, in cases where lensed images form close to individual galaxies, careful modeling of those individual galaxies is required to accurately reproduce the positions of nearby images. As our goal here is to obtain a good cluster-scale lens model instead of optimising individual galaxy mass distributions, we exclude image systems 2, 7, 13, 21, 24 and 27 in Caminha et al. (2017) (see their Fig. 1), whose multiple images fall very close to massive cluster member galaxies. This way we do not need to fine-tune every member galaxy with lensed images nearby and still maintain the accuracy of the large-scale cluster lens model.

We include cluster member galaxies as 128 dual pseudo-isothermal elliptical mass distributions (dPIE) (Eliásdóttir et al. 2007) located at their detected light centroids, with the ellipticity and position angle fixed to their observed values obtained from the Molino et al. (2017) catalog. The convergence of the dPIE profile is given by

$$\kappa_g = \frac{\sigma_{g,v}^2}{2G \Sigma_{cr}} \left(\frac{1}{R_{g,\epsilon}} - \frac{1}{\sqrt{R_{g,\epsilon}^2 + r_{g,t}^2}} \right), \quad (4)$$

Table 1. Mean lensing magnification of multiple images of Systems *A* and *B*. Calculated based on the fine-tuned lens model as described in Section 3.2.

Image	$\bar{\mu}$	Image	$\bar{\mu}$
A1	3.8	B1a	15.2
A2a	4.3	B1c	10.4
A2b	5.4	B1d	12.1
A2c	7.5	B1e	7.5
A3a	4.5	B2a	8.2
A3b	4.4	B2c	13.0
A3c	6.2	B2d	12.0
		B2e	8.4

where $r_{g,t}$ is the truncation radius. To reduce the total number of free parameters, we scale all 128 member galaxies with a constant mass-to-light ratio through

$$\sigma_{g,v} = \sigma_{g,v}^0 \left(\frac{L}{L_0} \right)^{\frac{1}{4}}, \quad r_{g,t} = r_{g,t}^0 \left(\frac{L}{L_0} \right)^{\frac{1}{4}}, \quad (5)$$

where L_0 is the reference luminosity with magnitude $m_{\text{F814W}} = 19.6$. Hence there are only two free parameters for member galaxies: $\sigma_{g,v}^0$ and $r_{g,t}^0$.

Constraints of this fiducial cluster lens model are po-

sitions of 72 multiple images from 21 background sources identified by [Caminha et al. \(2017\)](#), excluding image systems 2, 7, 13, 21, 24 and 27 for reasons described above. The optimization is performed based on object positions in the source plane. We obtain similar best-fit parameters as [Caminha et al. \(2017\)](#). The root-mean-square positional offset between observed and predicted images is $\langle \text{rms} \rangle_{\text{im}} = 0''.76$ in the image plane, averaged over all 72 images of 21 sources. The rms position offsets for Systems *A* and *B* are found to be $\langle \text{rms} \rangle_{\text{im}} = 0''.38$ and $\langle \text{rms} \rangle_{\text{im}} = 0''.73$, respectively. In the Appendix, we list the coordinates and redshifts of all 72 images used as constraints, as well as the best-fit model parameters.

3.2 Fine-tuned lens model for Systems *A* and *B*

Based on the fiducial cluster lens model described above, we now optimize the lens model for Systems *A* and *B* separately to ensure the highest accuracy in matching the observed locations of multiply-lensed images in these two systems. In the fiducial model, the respective centers of the three cluster-scale PIEMD halos are located at $\approx 2''$ from the brightest cluster galaxy (BCG), $\approx 13''$ northwest and $\approx 30''$ southeast of the BCG (see [Table A2](#) for a summary). As the southeast cluster-scale PIEMD halo occurs close to the lensed images of Systems *A* and *B*, we obtain a refined lens model, leaving all parameters of this PIEMD halo free while fixing the other two cluster-scale PIEMD halos to their best-fit parameters in the fiducial model. We also notice that three of the cluster member galaxies (marked as Gm1, Gm2 and Gm3 in [Figures 1 and 2](#)) are located close to some images of Systems *A* and *B*. We therefore allow the velocity dispersion $\sigma_{g,v}$ and truncation radius $r_{g,t}$ of these three cluster members to vary freely in the fine-tuned model optimization, instead of being scaled together with the rest of member galaxies. Finally, the external shear parameters are fixed to their best-fit values in the fiducial model.

Because we are particularly interested in accurately producing the lensing effect for Systems *A* and *B*, we also include constraints from the two substructures of *A3* (designated *A31* and *A32* in [Table A1](#)), and the fainter galaxy *B2* in System *B*, which are not used in [Caminha et al. \(2017\)](#). With a total of 18 multiple images of *A* and *B* as constraints (the first 18 entries in [Table A1](#)), we then run *LENSTOOL* again with the above set-up, and obtain a fine-tuned model. This model places significantly more weight on the local perturbers (Gm1, Gm2, and Gm3) and provides much improved root-mean-square positional offsets for the systems of interest in this study. The rms position offsets for Systems *A* and *B* are reduced to $\text{rms}_{\text{im}} = 0''.1$ and $\text{rms}_{\text{im}} = 0''.21$, respectively. The best-fit parameters are listed [Table A3](#) in the Appendix. In [Figures 1 and 2](#), we show the predicted critical curves by this fine-tuned model for sources at the redshifts of Systems *A* and *B*. Mean lensing magnification factors of multiple images of Systems *A* and *B* based on the fine-tuned lens model are presented in [Table 1](#). Wherever required in subsequent analyses, we use this fine-tuned model to derive image position deflections and magnifications.

4 ANALYSIS: GALAXY PROPERTIES

Both Systems *A* and *B* comprise two distinct components: (1) the continuum sources detected in the broadband *HST* images and (2) the Ly α emitting nebulae that are more spatially extended than the continuum sources and are only visible in the MUSE IFS data. Available broadband photometry and spectra of the galaxies provide important constraints for the star formation histories and the underlying stellar populations. In this section, we investigate the properties of the galaxies by analysing the photometric and spectroscopic data of the continuum sources. We will present the analysis of the associated Ly α emitting nebulae in [§5](#).

4.1 Photometric properties

Accurate photometric measurements of galaxies in Systems *A* and *B* are challenging due to the crowding of members of the lensing cluster and non-negligible intracluster light (e.g., [Figures 1 & 2](#)). We first measure broadband magnitudes of individual lensed images of each galaxy in different bandpasses using a combination of circular and isophotal apertures determined by SExtractor (v.2.19.5; [Bertin & Arnouts 1996](#)). These measurements (presented in the Appendix) are then corrected for lensing magnifications based on the fine-tuned lens model (see [Table 1](#) presented in [§3](#)).

For galaxies *A2* and *A3* in System *A*, their *b* images occur between two bright foreground galaxies, resulting in uncertain background subtraction in the photometric measurements. The de-magnified apparent magnitudes of *A2* and *A3* are therefore determined based on an average of images *a* and *c*. The de-magnified magnitudes of *A2* and *A3* in image *a* are ≈ 0.2 magnitudes fainter than that in image *c*, suggesting that the true magnification factor for image *a* relative to image *c* is smaller than what is predicted by the lens model. In [§5](#) below, we also show that the apparent Ly α surface brightness in the extended nebulae from image *a* is fainter than what is seen in images *b* and *c*, supporting a smaller relative magnification factor at the location of image *a*. Such a discrepancy in image brightnesses is commonly seen in strongly-lensed galaxies and quasars, and is often due to the limited accuracy of lens models and/or the presence of small-scale substructures in the lens (e.g. [McKean et al. 2007](#); [Hezaveh et al. 2016](#)). The discrepancy of ≈ 0.2 magnitudes seen here is within the typical scatter of $\gtrsim 25\%$ between de-lensed magnitudes of multiply-lensed galaxies in cluster lenses (e.g. [Lam et al. 2014](#); [Caminha et al. 2016a](#)). By averaging the de-lensed magnitudes between images *a* and *c*, we therefore mitigate the effect of lensing uncertainty on the magnification of these two galaxies.

Similarly, the *b* images of galaxies *B1* and *B2* are excluded due to the contamination from the nearby cluster member galaxy Gm3. In addition, image *e* of *B1* is unusually bright compared with its counter part in images *a*, *c* and *d*, which are between 0.8 and 1.2 magnitudes fainter than image *e* across different bandpasses after the lensing correction. Such an enhancement in brightness is not observed in image *e* of *B2*. This brightness anomaly of *B1e* can also be seen in the color image in [Figure 2](#), and may be attributed to magnification perturbation caused by unseen substructures local to *B1e* (e.g. [McKean et al. 2007](#); [Hezaveh et al. 2016](#)). Consequently, the de-magnified apparent magnitudes of *B1*

Table 2. Summary of galaxy photometry for System *A*^a.

	redshift	M_{1500}^b	F300W ^c	F390W	F435W	F475W	F606W	F625W
A1	3.0364	-21.52	> 26.14	25.85 ± 0.08	25.02 ± 0.03	24.59 ± 0.02	24.03 ± 0.07	23.90 ± 0.01
A2	3.0378	-19.87	> 28.37	26.97 ± 0.12	26.29 ± 0.05	26.10 ± 0.03	25.67 ± 0.04	25.43 ± 0.02
A3	3.0384	-19.63	> 28.57	27.53 ± 0.12	26.82 ± 0.05	26.46 ± 0.03	25.91 ± 0.04	25.76 ± 0.02
	F775W	F814W	F850LP	F105W	F110W	F125W	F140W	F160W
A1	23.76 ± 0.01	23.76 ± 0.01	23.73 ± 0.02	23.73 ± 0.01	23.71 ± 0.01	23.71 ± 0.01	23.52 ± 0.01	23.34 ± 0.01
A2	25.37 ± 0.02	25.32 ± 0.01	25.31 ± 0.03	25.47 ± 0.02	25.50 ± 0.01	25.54 ± 0.02	25.36 ± 0.01	25.32 ± 0.01
A3	25.66 ± 0.02	25.62 ± 0.01	25.61 ± 0.03	25.72 ± 0.02	25.70 ± 0.01	25.75 ± 0.02	25.51 ± 0.01	25.34 ± 0.01

^aAll magnitudes are de-magnified based on the lens model described in §3, and averaged among images *a* and *c*.

^bAt $z = 3$, typical star-forming galaxies have $M_{1500}^* = -21.1 \pm 0.2$ (e.g., Reddy et al. 2008)

^c 2σ UV flux upper limit, averaged among the F225W, F275W and F336W bandpasses.

Table 3. Summary of galaxy photometry for System *B*^a.

	redshift	M_{1500}^b	F450W ^c	F475W	F606W	F625W	F775W	F814W
B1	3.7540	-17.23	> 30.08	29.99 ± 0.20	29.15 ± 0.06	28.94 ± 0.08	28.69 ± 0.08	28.81 ± 0.05
B2	3.7540	-17.01	> 29.99	> 30.68 ^d	29.59 ± 0.11	29.57 ± 0.17	28.91 ± 0.11	28.95 ± 0.07
	F850LP	F105W	F110W	F125W	F140W	F160W		
B1	28.80 ± 0.11	29.29 ± 0.09	29.13 ± 0.05	29.19 ± 0.09	29.28 ± 0.08	29.22 ± 0.08		
B2	28.87 ± 0.15	29.15 ± 0.10	29.11 ± 0.06	29.12 ± 0.10	28.98 ± 0.07	28.83 ± 0.07		

^aAll magnitudes are de-magnified based on the lens model described in §3, and averaged among images *a*, *c* and *d*.

^bAt $z = 4$, typical star-forming galaxies have $M_{1500}^* = -21.1 \pm 0.1$ (e.g., Bouwens et al. 2007)

^c 2σ UV flux upper limit, averaged among the F225W, F275W, F336W, F390W and F435W bandpasses.

^d 2σ flux upper limit.

Table 4. SED fitting results, showing 16%–84% confidence interval for each parameter.

galaxy	redshift	$\log(M_{\text{star}}/M_{\odot})$	SFR ($M_{\odot} \text{ yr}^{-1}$)	Age (Gyr)	τ (Gyr)	A_V
A1	3.0364	[9.93, 9.98]	[89.84, 101.85]	[0.11, 0.14]	[1.37, 4.35]	[0.72, 0.77]
A2	3.0378	[8.95, 8.98]	[10.71, 11.45]	[0.05, 0.06]	[1.30, 4.38]	[0.62, 0.65]
A3	3.0384	[9.23, 9.27]	[13.02, 15.81]	[0.14, 0.19]	[1.44, 4.37]	[0.64, 0.71]
B1	3.7540	[7.59, 7.96]	[0.23, 0.40]	[0.13, 0.53]	[1.26, 4.25]	[0.05, 0.25]
B2	3.7540	[8.43, 8.72]	[0.50, 0.91]	[0.43, 1.31]	[1.31, 4.35]	[0.47, 0.74]

and *B2* are determined by averaging measurements of images *a*, *c* and *d*. Finally, Galactic extinction corrections are calculated using the NED Galactic Extinction Calculator³ and applied to the observed magnitudes in individual bandpasses following the Schlafly & Finkbeiner (2011) extinction map.

For galaxies in System *A* (*B*), the bandpasses bluer of F390W (F475W) correspond to rest-frame wavelengths $\lambda_{\text{rest}} < 912\text{\AA}$, and no fluxes are detected above the background noise. We therefore place a $2\text{-}\sigma$ upper limit of the observed flux in each of these bandpasses. Unfortunately, these images are not sufficiently sensitive to provide meaningful constraints for the escape fraction of ionizing photons from these galaxies. The final de-magnified apparent magnitudes of galaxies *A* and *B* in different bandpasses are pre-

sented in Tables 2 and 3, while the direct measurements of individual images are presented in Table B1 for reference.

To characterize the intrinsic luminosities of these galaxies, we also estimate the rest-frame UV absolute magnitudes at 1500 Å, M_{1500} , using the observed F606W (F775W) brightness for galaxies in System *A* (*B*). At the respective redshifts of Systems *A* and *B*, these bandpasses correspond roughly to the rest-frame 1500 Å, and provide a robust estimate of the intrinsic UV luminosity. The absolute magnitudes of *A1*, *A2*, *A3*, *B1* and *B2*, at rest-frame 1500 Å are found to be $M_{1500} = -21.52, -19.87, -19.63, -17.23$ and -17.01 , corresponding to 1.61, 0.35, 0.28, 0.03, 0.03 L_* , respectively, for a characteristic rest-frame absolute magnitude of $M_* = -21$ (e.g., Bouwens et al. 2007; Reddy et al. 2008).

³ https://ned.ipac.caltech.edu/extinction_calculator

4.2 Stellar population parameters

The observed broadband spectral energy distributions (SEDs) of galaxies in Systems *A* and *B* based on the photometric measurements presented in Tables 2 and 3 are typical of star-forming galaxies at $z = 3\text{--}4$ (e.g., Bouwens et al. 2007). To quantify the star formation histories, we perform a stellar population synthesis analysis using *Bayesian Analysis of Galaxies for Physical Inference and Parameter Estimation* (BAGPIPES, Carnall et al. 2018), which employs the 2016 version of the Bruzual & Charlot (2003) stellar synthesis models. We assume an exponentially declining star formation model, $\text{SFR}(t) \propto e^{-t/\tau}$, where τ represents the e-folding time and is a free parameter, and infer the stellar mass (M_{star}), star formation rate (SFR), age and dust extinction (A_V) of the continuum sources in both systems based on the observed SEDs from F606W to F160W. Because of a strong degeneracy between stellar age, metallicity, and dust attenuation (e.g., Conroy 2013), we impose a metallicity prior based on the mass-metallicity relation for high-redshift galaxies (e.g., Ma et al. 2016) and fix the metallicity of *A1* to 20% of the solar value, 10% for *A2* and *A3*, and 5% for *B1* and *B2*.

The 16%–84% confidence intervals in M_{star} , SFR, age, and A_V are presented in Table 4. All five galaxies are best characterized by a long star formation e-folding time that exceeds $\tau = 1$ Gyr, along with a relatively young, best-fit stellar age. In particular, the best-fit stellar ages for galaxies in System *A* are less than 200 Myr, making the adopted exponentially declining star formation model equivalent to a constant SFR scenario. This makes the inferred stellar age and SFR insensitive to the adopted star formation history, either exponentially declining or rising (Reddy et al. 2012). As discussed below, a constant star formation history is also consistent with the spectral features uncovered in the MUSE data. The inferred SFR for galaxies *A1*, *A2*, and *A3* range between 10 and 100 $M_{\odot} \text{yr}^{-1}$ and M_{star} between 10^9 and $10^{10} M_{\odot}$, typical of UV luminous star-forming galaxies at $z \approx 3$ (e.g. Shapley 2011). In contrast, galaxies *B1* and *B2* have significantly lower SFR and stellar mass with $M_{\text{star}} \approx 10^8 M_{\odot}$, more typical of Ly α emitters (LAE) at $z \approx 3$ with a characteristic star formation time scale of $\lesssim 1$ Gyr (e.g. Feltre et al. 2020).

4.3 Spectroscopic properties

At $z = 3\text{--}4$, available MUSE data cover the rest-frame wavelength range from $\lambda_{\text{rest}} > 1200 \text{ \AA}$ to $\lambda_{\text{rest}} < 1920 \text{ \AA}$, and provide additional constraints for the star-forming interstellar medium (ISM) and the stellar populations in Systems *A* and *B*. We extract individual galaxy spectra using spherical apertures centered on the location of the continuum sources, with varying sizes for different images depending on the intrinsic image size and magnification. Because galaxies *B1* and *B2* are blended in the ground-based MUSE data, we are only able to extract a single spectrum for these two galaxies. The extracted spectra (without lensing correction) are presented in Figure 3, along with the corresponding 1- σ error spectra. For galaxies *A2* and *A3*, the spectra shown are combined from images *a* and *c*, while image *b* is excluded due to possible contamination from nearby cluster member galaxies. Similarly for *B1* and *B2*, image *b* is excluded from the

combined spectrum due to possible contamination from the nearby elliptical galaxy. Note that the brightness anomaly of *B1e* described in §4.1 does not affect the spectral features due to the achromatic nature of lensing. Image *e* is therefore included in the combined spectrum.

The spectra of galaxies *A1*, *A2*, and *A3* are characterized by three distinct features: (1) a blue continuum consistent with the broadband photometry presented in Table 2; (2) strong interstellar absorption due to neutral hydrogen and heavy ions (marked in green, dotted line) that are commonly seen in $z \approx 3$ galaxies (e.g., Shapley et al. 2003; Erb et al. 2014), and (3) nebular emission lines due to He II λ 1640, O III] λ 1660, 1666, and C III] λ 1906, 1908, as well as excited Si II* λ 1264, 1309, and 1530 lines. The strong DLA features observed in the spectra of galaxies *A1*, *A2*, and *A3* reveal the presence of a significant amount of neutral gas in the ISM of these galaxies. A Voigt profile analysis of the red damping wing at the systemic redshifts of these galaxies (see below) yields best-fit HI column densities of $\log N(\text{HI})/\text{cm}^{-2} = 20.9 \pm 0.1$, 21.3 ± 0.1 , and 21.3 ± 0.1 for galaxies *A1*, *A2*, and *A3*, respectively, indicating a minimum surface neutral gas mass density of $\Sigma_{\text{gas}} = 8\text{--}20 M_{\odot} \text{pc}^{-2}$. The best-fit DLA profiles are presented in the top row of Figure 4. Note that the blue-side of the observed DLA profiles are contaminated by the forest of Ly α absorption lines in the foreground and therefore excluded from the fit.

Apart from the strong DLA features, the prominent C IV λ 1548, 1550 absorption profiles in galaxies *A1*–*3* show a blue tail extending beyond -2500 km s^{-1} , indicating the presence of stellar winds produced by massive young stars. The C IV λ 1548, 1550 lines are shown in the second and third rows of Figure 4. In addition, low-ionization absorption lines, such as C II λ 1334, Si II λ 1526 and Fe II λ 1608 as presented in the 4th–6th rows of Figure 4, indicate the presence of outflowing gas in the ISM of these galaxies. These absorption lines are clearly asymmetric with an extended blue wing in *A1*. A weak, extended blue wing is also visible in Fe II λ 1608 for *A2* and *A3*, while the core is more symmetrically distributed around the systemic velocity.

To quantify outflow velocities, we measure the absorption velocity centroid, v_{center} , and the maximum velocity of the absorption, v_{max} . Both quantities are measured with respect to the galaxy systemic velocities derived from nebular emission lines (see below). v_{center} is determined to be at the location of the deepest absorption trough. v_{max} measures the blueshifted velocity at which the absorption is consistent with the continuum to within 1- σ level. It is determined through the relation $f(v_{\text{max}}) = 1.0 - \delta(v_{\text{max}})$, where f is the continuum-normalised flux and δ is the associated flux error (e.g. Martin et al. 2012). To estimate the uncertainties of both v_{max} and v_{center} , we repeat the measurements on 1000 random Gaussian generations of the spectra based on the observed intensities and error arrays, and report the mean and standard deviation of the 1000 measured values for both quantities. In addition, to quantify the internal velocity width of the absorption features, we fit a Gaussian profile to the red side of the absorption feature that is redward of the measured v_{center} , and obtain a FWHM_{red} that is not affected by the extended blue wing. The model Gaussian profile is convolved with the instrument line spread function before fitting with the data.

Because both C II λ 1334 and Si II λ 1526 absorption lines

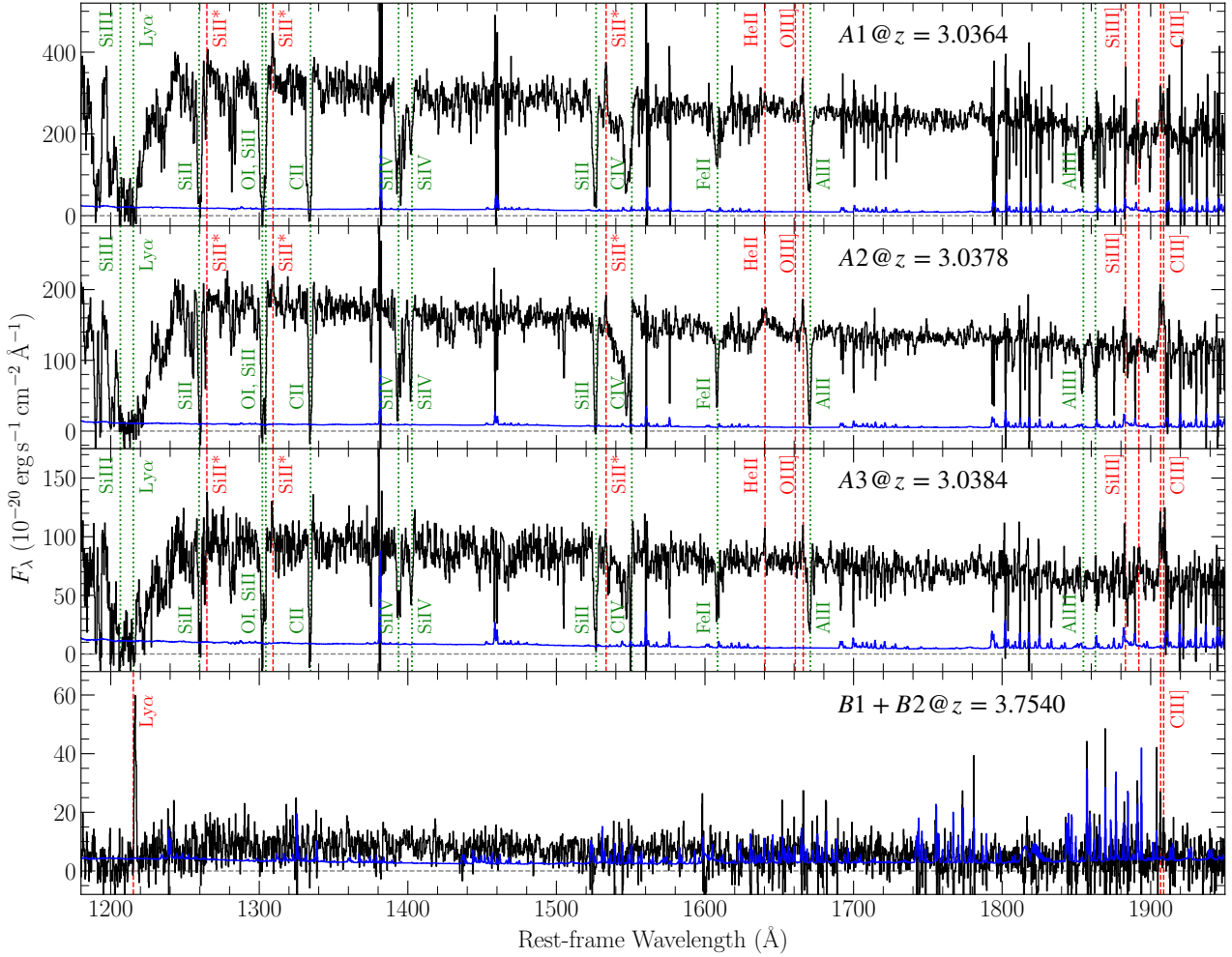


Figure 3. Sky-subtracted spectra of Systems *A* and *B* without lensing magnification corrections. For *A2* and *A3*, multiple images *a* and *c* are stacked. For *B1+B2* combined spectrum, images *a*, *c*, *d* and *e* are stacked. Rest-frame wavelength is calculated according to the best-fit redshift of each galaxy, as marked in their individual panels. The corresponding $1\text{-}\sigma$ error spectrum is shown in blue in each panel. Red dashed lines indicate major emission features while green dotted lines indicate major absorption features.

are saturated, we make the measurements using Fe II λ 1608 line. We find $[v_{\text{center}}, v_{\text{max}}, \text{FWHM}_{\text{red}}]$ of $[-42 \pm 58, -757 \pm 72, 474 \pm 52]$, $[-22 \pm 30, -614 \pm 147, 301 \pm 26]$ and $[-38 \pm 28, -480 \pm 140, 211 \pm 56]$ km s $^{-1}$ for *A1*, *A2* and *A3*, respectively. Both *A1* and *A2* exhibit an absorption velocity centroid consistent with $v = 0$ to within measurement uncertainties, while *A3* displays a slightly more significant blueshift. At the same time, the maximum velocity v_{max} of $\approx 500\text{--}760$ km s $^{-1}$ observed in Fe II λ 1608 exceeds the respective FWHM_{red} measured for these galaxies, clearly indicating the presence of high-velocity outflows. We also note that the measured FWHM_{red} is broader than the FWHM measured for nebular emission lines in all three galaxies (see below). In particular, for galaxy *A1*, the absorption line width is ≈ 3 times the width inferred from nebular emission lines (see Figure 4), suggesting the presence of turbulence ISM local to the star forming regions.

All three galaxies show significantly smaller outflow velocities in the line centroids in comparison to typical Ly α emitting galaxies, which is ~ 200 km/s as reported in (Shibuya et al. 2014). If the outflows originate in a biconi-

cal structure, the small outflow velocities in System *A* may suggest a large inclination angle of the cones of $\sim 80^\circ$, assuming that the mean v_{center} among the three galaxies of ~ 34 km/s is the projected velocity from an inclined cone flowing out with 200 km/s. Such a large inclination angle is also consistent with the side-lobe like morphology of the Ly α nebulae (i.e., the two clouds bracketing the continuum galaxies) and the elongated gap between the two clouds, as described below in §5.1. In addition, the fact that all three galaxies show similar uncharacteristically small outflow velocities might suggest that they all reside in the same outflow bubble likely originating from galaxy *A1*.

Different from galaxies in System *A*, galaxies *B1* and *B2* exhibit a strong Ly α emission with no apparent DLA trough, and resolved C III] $\lambda\lambda$ 1906, 1908 doublet features on top of a faint UV continuum. No strong absorption features are detected, but the spectrum does not have sufficient sensitivities for placing strong constraints. We measure a rest-frame equivalent width (EW_{rest}) of the Ly α emission line of galaxies *B1* and *B2* over the observed wavelength

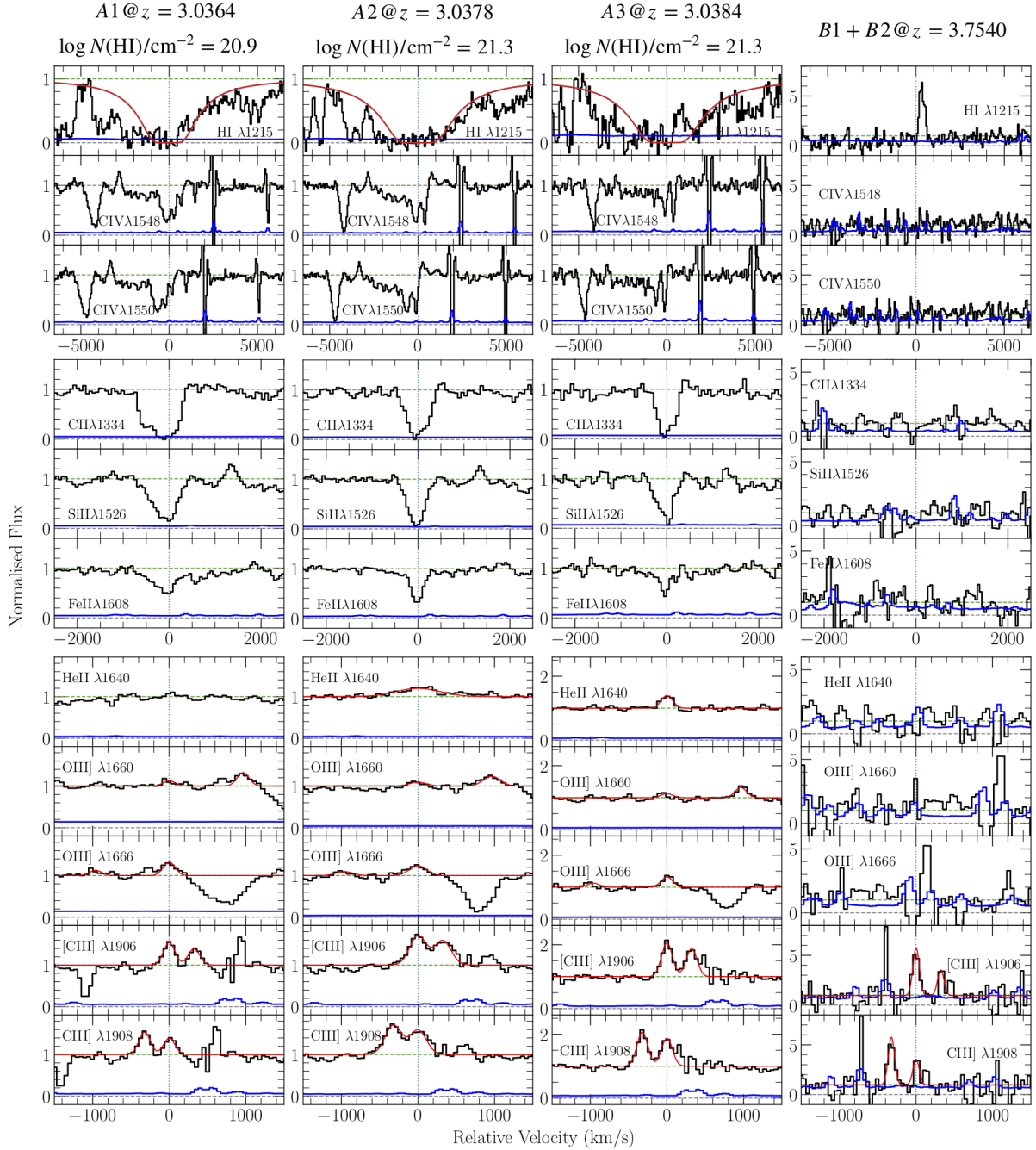


Figure 4. Summary of the ISM absorption and emission features of Systems *A* (left three columns) and *B* (right column). Zero velocity corresponds to the systemic redshift determined from nebular emission lines of each galaxy (see Table 5). The red curve in the H I panels shows the best-fit DLA profile with the estimated $N(\text{HI})$ displayed at the top of each column. At negative velocities, the DLA profiles are contaminated by the forest of Ly α absorption lines in the foreground. The C IV $\lambda\lambda$ 1548, 1550 absorption profiles are presented in the second and third rows, showing blue absorption tail extending beyond -2500 km s^{-1} . The 4th–6th rows show the low-ionization lines C II λ 1334, Si II λ 1526 and Fe II λ 1608, which exhibit asymmetric absorption profiles with extended blue tails, indicating the presence of gas outflows in the ISM. The best-fit Gaussian models of He II λ 1640, O III $\lambda\lambda$ 1660, 1666 and C III $\lambda\lambda$ 1906, 1908 emission lines are shown in red curves in bottom five rows. He II λ 1640 is fitted with a single Gaussian. The doublets are all fitted with a double Gaussian, and the separation between two Gaussian components is fixed by their rest-frame wavelength separation. We fix the flux ratio O III λ 1666/O III λ 1660 = 2.5. The redshift is tied to be consistent among all lines in each galaxy, and the best-fit values (shown at the top of each column) sets the zero velocity marked by the vertical dotted line. Data spectrum (continuum normalised) is shown in black, $1-\sigma$ error spectrum in blue and best-fit models in red. Flux and rest-frame equivalent width measured from the best-fit models for each emission line is listed in Table 5. While galaxies *B1/B2* display a strong Ly α and modest C III $\lambda\lambda$ 1906, 1908 emission features, the data quality is not sufficient to place meaningful constraints on He II, or O III]

window from $\lambda_1 = 5760 \text{ \AA}$ to $\lambda_2 = 5796 \text{ \AA}$, and obtain $\text{EW}_{\text{rest}}(\text{Ly}\alpha) = 33.3 \pm 1.5 \text{ \AA}$.

For all galaxies, we are able to determine an accurate systemic redshift for each of these galaxies by simultaneously fitting multiple emission lines with a Gaussian function, convolved with an appropriate instrument line spread function, which shares a common velocity centroid. Specifically for galaxies in System *A*, we adopt a single Gaussian model for $\text{He II } \lambda 1640$ and a double Gaussian model for both $\text{O III}] \lambda \lambda 1660, 1666$ and $\text{C III}] \lambda \lambda 1906, 1908$ doublets. In addition, the flux ratio of $\text{O III}] \lambda 1666 / \text{O III}] \lambda 1660$ is fixed at 2.5 as expected from their radiative transition probabilities. For galaxy *A1*, $\text{He II } \lambda 1640$ is excluded from the fitting due to the lack of detection, and $\text{O III}]$ and $\text{C III}]$ doublets are fitted with a common line width. For galaxy *A2*, $\text{He II } \lambda 1640$ is visibly broader than both $\text{O III}]$ and $\text{C III}]$ doublets. We therefore allow the width of $\text{He II } \lambda 1640$ to be a free parameter while the the doublets share a common line width in the fit for *A2*. The difference in line width between $\text{He II } \lambda 1640$ and $\text{O III}] / \text{C III}]$ doublets is not surprising, as $\text{He II } \lambda 1640$ emission is expected to have both stellar and nebular contributions which can sometimes lead to complex line structures (e.g. Berg et al. 2018; Kehrig et al. 2018; Nanayakkara et al. 2019; Feltre et al. 2020). For galaxy *A3*, fittings with or without $\text{He II } \lambda 1640$ line width being a free parameter return consistent results within uncertainties. Therefore, we assign a common line width to all lines fitted for *A3* for simplicity.

For galaxies *B1* and *B2*, we fit a double Gaussian model with a fixed doublet separation to the $\text{C III}] \lambda \lambda 1906, 1908$ intercombination lines. The best-fit redshifts, line widths, integrated line fluxes, and EW_{rest} , along with associated errors of individual galaxies are presented in Table 5. The best-fit line profiles of the emission features are also presented in Figure 4.

4.4 Emission line diagnostics

The UV emission line properties presented in Table 5 are typical of star-forming galaxies at $z \approx 3$ (e.g., Maseda et al. 2017; Nanayakkara et al. 2019; Feltre et al. 2020), and reveal a turbulent and high-density nature in the ISM with a radiation field dominated by massive young stars in these galaxies. The best-fit FWHMs of the emission lines correspond to velocity dispersions of $\approx 60 \text{ km s}^{-1}$ in *A1* and *A3*, and $\approx 100 \text{ km s}^{-1}$ in *A2*, which are within the typical range measured for $z = 2\text{--}3$ galaxies (e.g., $108 \pm 86 \text{ km s}^{-1}$ reported in Erb et al. 2006, and $\approx 50\text{--}150 \text{ km s}^{-1}$ reported in Kulas et al. 2012). The ratio between the $\text{C III}]$ intercombination lines serves as an important UV diagnostic of the electron density, n_e , in the ISM, although it saturates at density below $n_e \approx 10^3 \text{ cm}^{-3}$ (e.g., Kewley et al. 2019). The observed $[\text{C III}] \lambda 1906 / \text{C III}] \lambda 1908$ ratios of these galaxies range from 1.2 ± 0.2 for *A2* and *A3* to 1.9 ± 0.6 for *B1* and *B2*, constraining the ISM electron density in both Systems *A* and *B* to be $\lesssim 2 \times 10^4 \text{ cm}^{-3}$ for a gas temperature of 10,000 K (Osterbrock & Ferland 2006). The high-density limits are also comparable to what is seen in $\text{C III}]$ emitters at $z \approx 3$ (e.g., Maseda et al. 2017). In addition, the detection of $\text{He II } \lambda 1640$ emission, along with the presence of a prominent P-Cygni profile in $\text{C IV } \lambda \lambda 1548, 1550$ with blue absorption tail extending beyond $|\Delta v| \approx 2000 \text{ km s}^{-1}$ (second and third rows in Figure 4), indicate the presence of massive young stars

Table 5. Emission line fitting results, with lensing magnification corrected in all flux measurements based on mean magnification values listed in Table 1.

<i>A1</i> at $z = 3.0364 \pm 0.0001^a$			
	FWHM (km s^{-1})	Flux ($10^{-20} \text{ erg s}^{-1} \text{ cm}^{-2}$)	$\text{EW}_{\text{rest}}^b$ (\AA)
$\text{He II } \lambda 1640$		$< 45^c$	$< 0.18^d$
$\text{O III}] \lambda 1660$	147 ± 34	35 ± 9	0.14 ± 0.04
$\text{O III}] \lambda 1666$...	86 ± 22	0.36 ± 0.11
$[\text{C III}] \lambda 1906$...	120 ± 30	0.64 ± 0.19
$\text{C III}] \lambda 1908$...	87 ± 25	0.47 ± 0.16
<i>A2</i> at $z = 3.0378 \pm 0.0001^e$			
$\text{He II } \lambda 1640$	673 ± 83^f	49 ± 7	0.79 ± 0.13
$\text{O III}] \lambda 1660$	237 ± 14	9 ± 1	0.5 ± 0.02
$\text{O III}] \lambda 1666$...	22 ± 2	0.37 ± 0.05
$[\text{C III}] \lambda 1906$...	58 ± 4	1.23 ± 0.10
$\text{C III}] \lambda 1908$...	48 ± 3	1.02 ± 0.09
<i>A3</i> at $z = 3.0384 \pm 0.0001$			
$\text{He II } \lambda 1640$	136 ± 9	13 ± 2	0.41 ± 0.10
$\text{O III}] \lambda 1660$...	4 ± 1	0.13 ± 0.02
$\text{O III}] \lambda 1666$...	10 ± 1	0.34 ± 0.04
$[\text{C III}] \lambda 1906$...	32 ± 2	1.20 ± 0.10
$\text{C III}] \lambda 1908$...	26 ± 1	0.99 ± 0.08
<i>B1/B2</i> at $z = 3.7540 \pm 0.0001$			
$[\text{C III}] \lambda 1906$	43 ± 20	0.9 ± 0.2	3.36 ± 0.54
$\text{C III}] \lambda 1908$...	0.5 ± 0.2	1.80 ± 0.53

^a Obtained from a simultaneous fit of $\text{O III}] \lambda \lambda 1660, 1666$ and $\text{C III}] \lambda \lambda 1906, 1908$

^b Rest-frame equivalent width

^c $2\text{-}\sigma$ upper limit

^d $2\text{-}\sigma$ upper limit

^e Obtained from a simultaneous fit of all lines listed; same for *A3* and *B1/B2*

^f FWHM of $\text{He II } \lambda 1640$ in *A2* is not tied with other lines due to its wide line width

with $M \gtrsim 30 M_{\odot}$ (e.g., Leitherer et al. 1999; Pettini et al. 2000; Crowther 2007; Brinchmann et al. 2008; Cabanac et al. 2008). The presence of broad $\text{He II } \lambda 1640$ emission line in *A2* is also a sign of Wolf-Rayet stars that have a short lifetime of $\sim 5 \text{ Myr}$ (e.g. Schaerer & Vacca 1998; Crowther 2007; Cabanac et al. 2008), in agreement with the constant SFR scenario suggested by photometric SED analysis (see Table 4 and discussion in §4.2).

Finally, we investigate the possibility of these galaxies hosting an active galactic nucleus (AGN) using emission line diagnostics in the UV. Specifically, Feltre et al. (2016) shows that the combination of collisionally excited nebular lines $\text{O III}] \lambda \lambda 1660, 1666$, $\text{C III}] \lambda \lambda 1906, 1908$ and the $\text{He II } \lambda 1640$ recombination line can serve as a good indicator of the ISM ionization state. We compute the expected line ratios of $\text{O III}] \lambda \lambda 1660, 1666 / \text{He II } \lambda 1640$ and $\text{C III}] \lambda \lambda 1906, 1908 / \text{He II } \lambda 1640$ under different AGN and star formation (SF) ionization radiation fields, using the CLOUDY code (version 17.01; Ferland et al. 2017). For the AGN spectrum, we adopt the model continuum specified in CLOUDY with an effective temperature of 10^6 K , an X-ray to UV

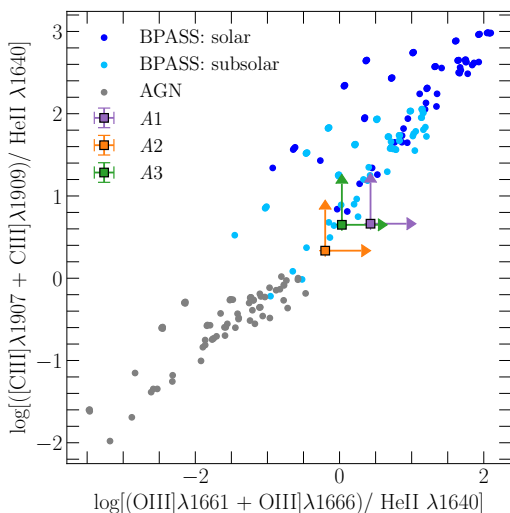


Figure 5. UV diagnostic diagram between AGN- (grey points) and stellar-dominated (blue and cyan points) radiation fields described in Section 4.4. Gas metallicities range from subsolar $Z = 0.002$ to supersolar $Z = 0.04$. The observed line ratios for galaxies A1, A2, and A3 are shown in squares. All three galaxies exhibit line ratios that are consistent with young stars (rather than AGN) dominating the ISM radiation field.

ratio of $\alpha_{\text{ox}} = -1.4$, a UV slope of $\alpha_{\text{uv}} = -0.5$ and an X-ray slope of $\alpha_{\text{x}} = -1$. For the SF model, we consider two stellar populations with sub-solar ($Z = 0.001$) and solar ($Z = 0.02$) metallicity, respectively. We use the FSPS code (v3.1; Conroy et al. 2009; Conroy & Gunn 2010) to generate a composite SF spectrum at the age of 250 Myr with BPASS models, which assumes a Salpeter stellar initial mass function with an upper mass cutoff at $100M_{\odot}$ (Eldridge et al. 2017). For each adopted AGN or SF spectrum, we generate a grid of models for the expected line ratios with the following parameters: gas metallicity $Z = [0.002, 0.02, 0.04]$, hydrogen density $n_{\text{H}}/\text{cm}^{-3} = [10, 10^2, 10^3, 10^4]$ and ionization parameter $U = [-4, -3.5, -3, -2.5, -2, -1.5]$. We set a temperature floor of 10,000 K. The predicted line flux ratios are shown in Figure 5, along with the observed values for galaxies A1, A2, and A3. The non-detection of He II $\lambda 1640$ in galaxy A1 naturally leads to lower limits of both line flux ratios. We also treat the line flux ratios in both A2 and A3 as lower limits because of a possible stellar contribution to the measured He II $\lambda 1640$ flux.

Figure 5 shows that all three galaxies in System A are consistent with an ISM radiation field being dominated by massive young stars and that there is no evidence of an AGN dominating the radiation field in these galaxies. Furthermore, the lack of C IV $\lambda 1548, 1550$ in emission also suggests the absence of AGN as C IV $\lambda 1548, 1550$ emission is expected to be prominent with a hard ionization background (e.g. Gutkin et al. 2016). Due to the lack of relevant emission lines in the combined spectrum of B1 and B2, we cannot conduct the same exercise for System B. A close examination of available deep X-ray data taken by *Chandra* also shows that there is no apparent excess of X-ray signal at the locations of Systems A and B.

5 ANALYSIS: LY α NEBULA PROPERTIES

The observed broadband photometric and spectroscopic properties of galaxies in System A indicate that these galaxies are typical of UV continuum selected star-forming galaxies at $z \approx 3$ with an ISM radiation field dominated by massive young stars, while galaxies in System B display properties that resemble low-mass LAEs in the early epoch. The large amount of ISM gas revealed in the spectra of galaxies A1, A2, and A3, coupled with a wide-spread Ly α nebula revealed in the MUSE data shows that this is a particularly gas-rich system. Here we present an analysis of the morphologies and line profiles of the extended Ly α nebulae in these two systems.

5.1 Pseudo narrow-band Ly α image and source plane reconstruction

To characterize the extended Ly α nebulae in both systems, we first form a pseudo narrow-band Ly α image for each system. We first note that all three galaxies in System A exhibit asymmetric Ly α emission feature within the DLA trough, with an enhanced red peak at $\Delta v \approx +500 \text{ km s}^{-1}$ (e.g., top row of Figure 4) from the respective systemic redshifts. The observed asymmetric profile of these emergent Ly α photons is similar to what is seen in the extended nebulae (see §5.2 below) and is characteristic of large-scale outflows that have been commonly identified in high-redshift galaxies (e.g. Franx et al. 1997; Frye & Broadhurst 1998; Pettini et al. 2000; Frye et al. 2002; Cabanac et al. 2008). An origin of the emergent Ly α photons in outflows is qualitatively consistent with the presence of gas outflows seen in absorption lines in galaxy spectra and the presence of massive young stars inferred from the UV spectral properties of the galaxies described in §4.4 (see also Pettini et al. 2000; Cabanac et al. 2008, for examples). Given the uncertainty of the line-of-sight distance between the galaxies and the Ly α emission location, whether these photons originate in the star-forming ISM of the galaxies or in the extended nebulae that are blended with the galaxy image by projection remains uncertain. Therefore, we construct two versions of the pseudo narrow-band Ly α image for System A: one without including the emergent Ly α photons in the DLA trough of the continuum sources, and a second one which incorporates both the Ly α photons in the DLA troughs and those in the extended nebulae. As discussed below and shown in Figures 6 and 7, this exercise enables a clearer understanding of the differences in the observed surface brightness profiles between multiple images, as well as establishing a direct connection between the galaxies and the line-emitting gas at large distances.

To construct a pseudo narrow-band Ly α image for System A without including the Ly α photons from the DLA troughs, we perform a local continuum subtraction per spaxel within the Ly α line. We determine a wavelength-dependent continuum level based on a linear interpolation of the continuum fluxes observed on the blue and red sides of the Ly α line. Specifically, we determine a medium flux over a spectral window of 4830-4863 Å on the blue side and a median flux over 4961-4994 Å on the red side. At $z \approx 3.04$, these correspond roughly to $[-5000, -3000]$ and $[+3000, +5000]$ km/s from the Ly α centroid (see Figure 10 below). The in-

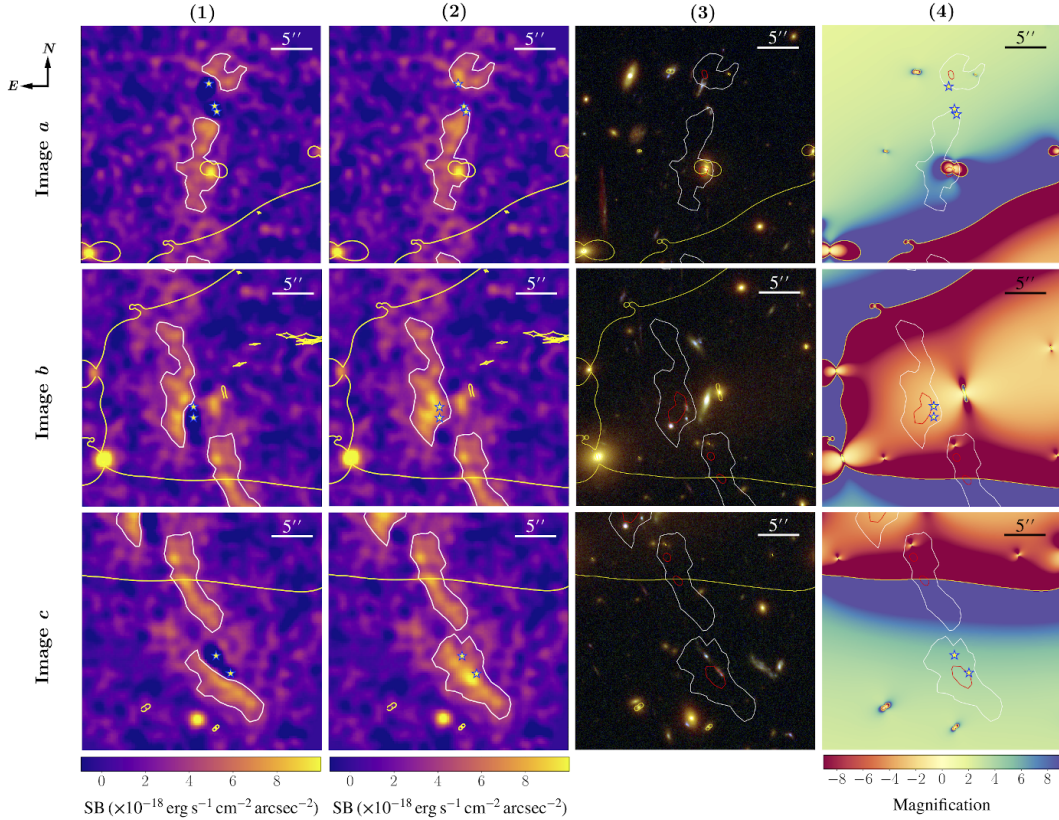


Figure 6. Summary of the lensing configuration of the observed Ly α arc in System A. Column (1): pseudo narrow-band images without the emergent Ly α flux within the DLA troughs at the locations of galaxy continuum. The images have been smoothed using a Gaussian kernel of $\text{FWHM}_{\text{smooth}} = 1''$. The contour marks constant surface brightness of $3.7 \times 10^{-18} \text{ erg s}^{-1} \text{ cm}^{-2} \text{ arcsec}^{-2}$, which is detected at the $3\text{-}\sigma$ level of significance in the smoothed image. Star symbols mark the positions of the associated star-forming galaxies identified in *HST* images. Column (2): same as Column (1) but includes Ly α flux from the DLA troughs at the locations of galaxy continuum (see text). Column (3): contours of multiply-lensed Ly α nebulae determined from Column (2) overlaid on individual galaxy images in the *HST* data to illustrate the relative alignment between star-forming regions and the line-emitting gas (see also Figure 1). Ly α surface brightness contours of $3.7 \times 10^{-18} \text{ erg s}^{-1} \text{ cm}^{-2} \text{ arcsec}^{-2}$ and $7.3 \times 10^{-18} \text{ erg s}^{-1} \text{ cm}^{-2} \text{ arcsec}^{-2}$ are shown in white and red, respectively, and the yellow contours mark the critical curves of the cluster lens for sources at $z = 3.038$. Column (4): the magnification map overlaid with the same Ly α contours to illustrate the spatial variation of lensing magnification across the nebulae. Negative magnification factors indicate flipped parity of the image.

terpolated value is then subtracted from the observed flux at each spaxel. A pseudo narrow-band image of the Ly α emission is then created by integrating the flux of each spaxel over the wavelength range from 4890 Å to 4930 Å, where Ly α flux is detected at a high level of significance (see Figure 10 below). A smoothed pseudo narrow-band Ly α image, using a Gaussian kernel of $\text{FWHM}_{\text{smooth}} = 1''$, is presented in Column (1) of Figure 6, which shows two nebulae separated roughly by $\approx 2''$ in the image plane and bracketing galaxies A1, A2, and A3 from the north and south. Furthermore, at the locations of galaxy continuum, there is a net absorption in this pseudo narrow-band image due to the presence of DLAs.

Next, we construct a pseudo narrow-band image that includes the emergent Ly α photons in the DLA troughs. This is accomplished by first identifying the spaxels within the continuum emitting regions of galaxies A1, A2, and A3 as defined by SExtractor (see §4.1). We then adopt the best-fit DLA model profile for each galaxy presented in Figure 4, and multiply the model by the best-fit continuum obtained using a low-order polynomial fit to line-free regions

in the integrated continuum spectrum presented in Figure 3. Next, the combined DLA-continuum model spectrum is scaled to match the continuum level of the spectrum in each spaxel and subtracted from the data. The amplitude of the continuum model for each spaxel is determined using the spectrum in the wavelength window from 5430 Å to 5560 Å, corresponding to rest-frame wavelengths from 1345 Å to 1375 Å, where no narrow-line features are present. The resulting difference data cube is combined with the previous continuum-subtracted data cube in the extended nebula region. A pseudo narrow-band image is then created by integrating over the wavelength range from 4890 Å to 4930 Å. Similarly, we smooth the image using a Gaussian kernel of $\text{FWHM}_{\text{smooth}} = 1''$, and present the smoothed pseudo narrow-band image in Column (2) of Figure 6.

In both versions of the pseudo narrow-band image presented in Columns (1) and (2) of Figure 6, the white contours mark a constant Ly α surface brightness of $3.7 \times 10^{-18} \text{ erg s}^{-1} \text{ cm}^{-2} \text{ arcsec}^{-2}$, which is detected at the $3\text{-}\sigma$ level of significance. A strong variation in Ly α surface brightness is clearly seen across both the northern and southern

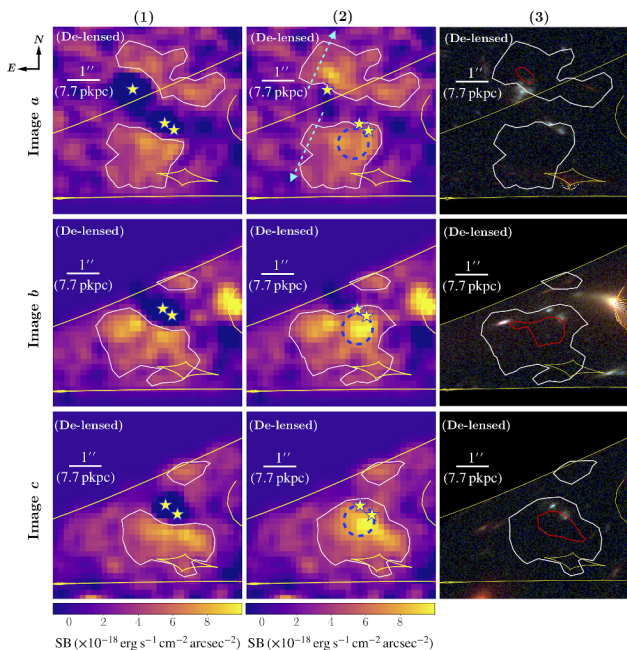


Figure 7. Column (1): de-lensed narrow-band image without Ly α flux from the DLA troughs at the locations of galaxy continuum. The images are smoothed using a Gaussian kernel of $\text{FWHM}_{\text{smooth}} = 0.5''$ in the source plane. The contour marks constant surface brightness of $3.7 \times 10^{-18} \text{ erg s}^{-1} \text{ cm}^{-2} \text{ arcsec}^{-2}$, corresponding to the $3\text{-}\sigma$ level of significance detected in the image plane, same as contours shown in Column (1) of Figure 6. Star symbols mark the de-lensed positions of the associated star-forming galaxies identified in *HST* images. Column (2): same as Column (1) but includes Ly α flux from the DLA troughs at the locations of galaxy continuum. Column (3): de-lensed Ly α contours overlaid on de-lensed *HST* data, with the yellow contours showing the caustics in the source plane. The blue dashed circles in Column (2) mark the apertures for the template spectrum extraction, which we use for the shell model analysis (see §5.3). The cyan dashed arrows show the directions along which we extract the one-dimensional surface brightness profile (see Figure 9 below)

nebulae, suggesting large spatial fluctuations in the underlying gas properties. While there exists a clear gap between the northern and southern nebulae, after including the Ly α signal inside the DLA troughs, the overlap between the constant Ly α surface brightness contours and these galaxies supports a continuous flow of dense gas from star-forming regions into a low-density halo environment. Furthermore, the surface brightness of the southern nebula in the vicinity of the galaxy continuum in images *b* and *c* is relatively more enhanced than that in image *a* after incorporating the Ly α signal in the DLA troughs (also see Figures 7 and 9 below). Specifically, in Column (2) of Figure 6, the Ly α surface brightness in image *a* in the vicinity of galaxies *A2* and *A3* is fainter by $\approx 25\%$ compared with images *b* and *c*. The reduced Ly α surface brightness in images *a* suggests that the magnification factor of image *a* relative to images *b* and *c* is smaller than what is predicted by the lens model. Such a difference in surface brightness of lensed Ly α nebulae is also seen in [Caminha et al. \(2016b\)](#), and is consistent with the discrepancy in de-lensed continuum brightnesses of *A2*

and *A3*, for which image *a* is fainter by ≈ 0.2 magnitude (see discussion in §4.1).

In Column (3) of Figure 6, Ly α surface brightness contours showing $3.7 \times 10^{-18} \text{ erg s}^{-1} \text{ cm}^{-2} \text{ arcsec}^{-2}$ and $7.3 \times 10^{-18} \text{ erg s}^{-1} \text{ cm}^{-2} \text{ arcsec}^{-2}$ (i.e., $3\text{-}\sigma$ and $6\text{-}\sigma$ determined from the pseudo narrow-band image shown in Column 2) are overlaid on top of the *HST* composite image from Figure 1. Note that image *b* is north-south flipped from images *a* and *c* in this lensing configuration. As a guide, we include the magnification map in Column (4) of Figure 6 (negative magnification factors indicate flipped parity of the image), overlaid with the same Ly α contours.

Through the deflection field calculated using the fine-tuned lens model (see §3.2), we de-lens both the pseudo narrow-band image and the *HST* images back to the source plane. The de-lensed pseudo narrow-band image smoothed with a Gaussian kernel of $\text{FWHM}_{\text{smooth}} = 0.5''$ in the source plane is presented in Columns (1) and (2) of Figure 7 for before and after including Ly α emission in the DLA troughs, respectively. The reconstructed source-plane images clearly show that most of the northern nebula is merely singly-lensed like galaxy *A1*, while the southern nebula stretches across the lensing field with rapidly changing magnification factors. Image *a*, covering the full extent of the nebulae in the source plane, constrains the projected size of the Ly α nebulae to approximately 30 pkpc from north to south. The de-lensed *HST* broadband images, as shown in Columns (3), are in excellent agreement among three multiple images, consistent with the low image position dispersion of $\text{rms}_{\text{im}} = 0''.1$ predicted by the fine-tuned lens model (see §3). The de-lensed pseudo narrow-band images show the same surface brightness discrepancy between multiple images as seen in the image plane (see Figure 6), where the surface brightness near the galaxy continuum regions is fainter in image *a* as discussed above. The white and red contours in Figure 7 correspond to surface brightnesses of $3.7 \times 10^{-18} \text{ erg s}^{-1} \text{ cm}^{-2} \text{ arcsec}^{-2}$ and $7.3 \times 10^{-18} \text{ erg s}^{-1} \text{ cm}^{-2} \text{ arcsec}^{-2}$, same as the contours shown in Figure 6.

When computing the total Ly α flux in the nebulae, we consider image *a* for the northern nebula to avoid the confusion of partially lensed multiple images, and average images *a* and *c* for the southern nebula. Due to the contamination from a nearby galaxy at the east side of the southern nebula in image *b*, we leave out image *b* in the average. In contrast with the continuum sources, the Ly α nebulae span a much larger area in the image plane, within which the magnification factor can vary significantly (see Column (4) of Figure 6). Therefore, instead of using a mean magnification factor, we correct the lensing magnification for each spaxel within the extended nebulae before summing over all spaxels within the $3\text{-}\sigma$ contour for these images. We then integrate the flux over the wavelength range of 4890–4930 Å (the same wavelength window for constructing the narrow-band image described above). The total de-lensed Ly α flux of the southern nebula obtained from image *a* is $\approx 5\%$ (25%) lower than that from image *c* before (after) including the Ly α flux from the DLA troughs. This difference of Ly α flux between images *a* and *c* is in agreement with what is observed in the Ly α surface brightness and de-lensed magnitudes of galaxies *A2* and *A3* (see §4), suggesting again that the magnification

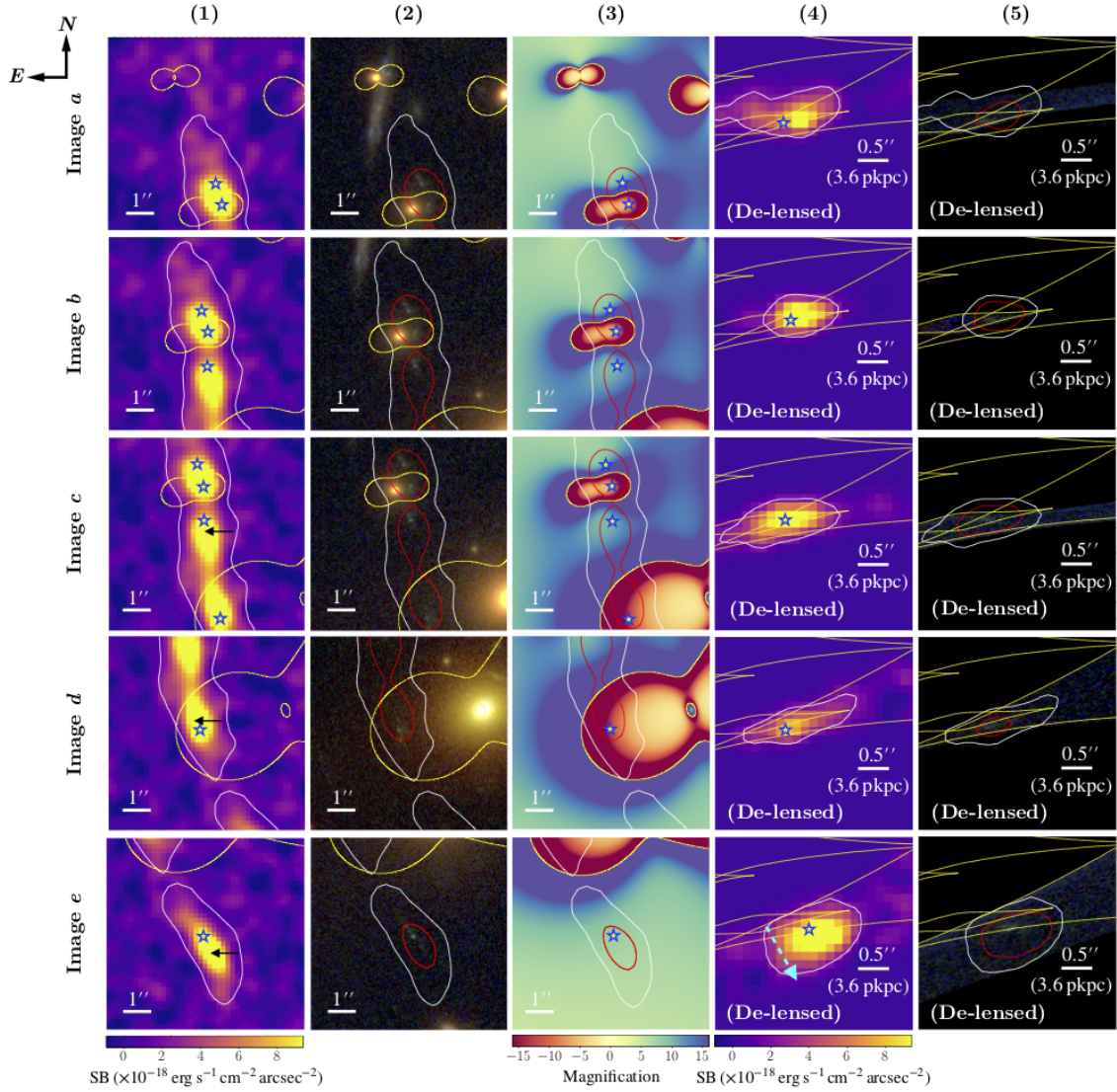


Figure 8. Summary of the lensing configuration of the observed Ly α arc in System *B*. Column (1): pseudo narrow-band image of the Ly α emission, smoothed with a Gaussian kernel of $\text{FWHM}_{\text{smooth}} = 1''$. The contour marks constant surface brightness of $2.8 \times 10^{-18} \text{ erg s}^{-1} \text{ cm}^{-2} \text{ arcsec}^{-2}$, which is detected at the $3\text{-}\sigma$ level of significance. Star symbols mark the positions of the associated star-forming galaxies identified in *HST* images, and the yellow contours show the critical curve for a source at $z_{\text{sys}} = 3.754$. Black arrows in the bottom three panels indicate the location of the brightest pixels in images c, d and e (one pixel from each image) that are included in the template Ly α spectrum used for shell model analysis (see §5.3). Column (2): contours of multiply-lensed Ly α nebulae overlaid on individual galaxy images in the *HST* data. Ly α surface brightness contours of $2.8 \times 10^{-18} \text{ erg s}^{-1} \text{ cm}^{-2} \text{ arcsec}^{-2}$ and $7.5 \times 10^{-18} \text{ erg s}^{-1} \text{ cm}^{-2} \text{ arcsec}^{-2}$ are shown in white and red, respectively. Column (3): the magnification map overlaid with the same Ly α contours to illustrate the spatial variation of lensing magnification across the nebulae. Column (4): de-lensed narrow-band image, smoothed with a Gaussian kernel of $\text{FWHM}_{\text{smooth}} = 0.5''$ in the source plane. White contours mark constant surface brightness of $2.8 \times 10^{-18} \text{ erg s}^{-1} \text{ cm}^{-2} \text{ arcsec}^{-2}$, corresponding to the $3\text{-}\sigma$ level of significance detected in the image plane, same as contours shown in Column (1). Column (5): de-lensed Ly α contours overlaid on de-lensed *HST* data, with the yellow contours showing the caustics in the source plane. White and red contours mark the 3- and $8\text{-}\sigma$ Ly α surface brightness, same as the contours in Column (2). The cyan dashed arrow shows the direction along which we extract the one-dimensional surface brightness profile (see Figure 9 below). Compared with System *A*, the lensing configuration of System *B* is much more complicated, with images *a-d* being partial images with different levels of completeness. Image *e* is the only complete image of Ly α emission above $3\text{-}\sigma$ limiting surface brightness.

factor near the continuum regions in image *a* is smaller than what is predicted by the lens model.

After excluding the Ly α flux from within the DLA troughs and correcting the lensing magnification, we obtain a total flux of $f_{\text{Ly}\alpha}(A_{\text{north}}) = (2.0 \pm 0.1) \times 10^{-17} \text{ erg s}^{-1} \text{ cm}^{-2}$ for the northern nebula, and $f_{\text{Ly}\alpha}(A_{\text{south}}) = (2.9 \pm 0.1) \times 10^{-17} \text{ erg s}^{-1} \text{ cm}^{-2}$ for the southern nebula. Including the

Ly α flux from the DLA troughs, the total flux is increased to $f_{\text{Ly}\alpha}^{\text{tot}}(A_{\text{north}}) = (2.7 \pm 0.1) \times 10^{-17} \text{ erg s}^{-1} \text{ cm}^{-2}$ for the northern nebula, and $f_{\text{Ly}\alpha}^{\text{tot}}(A_{\text{south}}) = (3.8 \pm 0.1) \times 10^{-17} \text{ erg s}^{-1} \text{ cm}^{-2}$ for the southern nebula. The Ly α signal inside the DLA troughs therefore accounts for $\approx 25\%$ of the total Ly α emission from both the northern and southern nebulae. At $z \approx 3.038$, these flux measurements (including

the Ly α flux in the DLA troughs) correspond to a Ly α luminosity of $L_{\text{Ly}\alpha}(A_{\text{north}}) = (2.15 \pm 0.07) \times 10^{42} \text{ erg s}^{-1}$ for the northern nebula, and $L_{\text{Ly}\alpha}(A_{\text{south}}) = (3.03 \pm 0.08) \times 10^{42} \text{ erg s}^{-1}$ for the southern nebula. Combining both northern and southern nebulae together leads to a total Ly α luminosity of $L_{\text{Ly}\alpha}(A) = (5.2 \pm 0.1) \times 10^{42} \text{ erg s}^{-1}$.

For System *B*, no apparent DLA or strong ISM absorption features are detected in the MUSE spectra of the star-forming regions, but the low S/N as a result of a faint continuum makes gas column density estimates highly uncertain. The apparent discontinuity in the continuum blueward and redward of the Ly α emission line is consistent with the expectation from the Ly α forest in the intergalactic medium at $z \approx 3.75$ (e.g. Becker et al. 2007). To construct a pseudo narrow-band image for this system, we first subtract the expected continuum at the observed Ly α line. Following the approach described above for System *A*, we determine the continuum level in each spaxel of the star-forming regions by matching the low-order polynomial fit of the UV continuum presented in Figure 4 to the observed spectrum. For spaxels outside of the continuum emitting regions, the continuum level at the Ly α emission line is determined based on a linear interpolation between blue and red continuum fluxes observed within 5730–5760 Å and 5800–5830 Å, respectively. A pseudo narrow-band image is then constructed by integrating the flux in the wavelength range from 5766 Å to 5796 Å. A smoothed version using a Gaussian kernel of FWHM = 1'' is presented in Column (1) of Figure 8, overlaid with constant surface brightness contours of $2.8 \times 10^{-18} \text{ erg s}^{-1} \text{ cm}^{-2} \text{ arcsec}^{-2}$ detected at $3\text{-}\sigma$. In Column (2) of Figure 8, contours of 2.8 and $7.5 \times 10^{-18} \text{ erg s}^{-1} \text{ cm}^{-2} \text{ arcsec}^{-2}$ (i.e., $3\text{-}\sigma$ and $8\text{-}\sigma$) are presented along with the *HST* composite image to illustrate the relative alignment between the Ly α nebulae and the associated galaxies. The magnification map presented in Column (3) shows the fast changing magnification factors across all five lensed images in System *B*, as the lensed Ly α emitting regions straddles multiple critical curves in the image plane. De-lensed Ly α pseudo narrow-band images (smoothed using a Gaussian kernel of FWHM = 0''.5) and the *HST* images in the source plane, based on the fine-tuned lens model described in § 3.2, are also presented in Columns (4) and (5) of Figure 8, respectively. Compared with System *A*, the lensing configuration of System *B* is more complicated, with images *a*–*d* being partial images of different completeness levels. Image *e* is the only complete lensed image of the Ly α nebula defined at the $3\text{-}\sigma$ level of significance in surface brightness. The source plane reconstruction from image *e* reveals a relatively symmetric Ly α emission morphology, roughly centered near the UV continuum sources. Using image *e*, we estimate the projected size of the Ly α emitting nebula to be approximately 10 pkpc in diameter. A small spatial offset, $\approx 0''.1$, is seen between UV continuum sources and the peak of Ly α emission, corresponding to ≈ 0.7 pkpc at $z = 3.754$. It is commonly observed among LAEs that the Ly α emission signals can have an offset from the UV continuum, with a median 1D projected offset of ≈ 0.6 pkpc in previous slit spectroscopic data (e.g., Hoag et al. 2019; Ribeiro et al. 2020; Lemaux et al. 2020). Larger offsets have also been found in narrow-band imaging data (e.g., Shibuya et al. 2014). However, we note that the continuum fluxes of

galaxies *B1* and *B2* are much fainter than the LAEs considered in those studies.

We use image *e*, the most complete image among all five multiple images of System *B*, to compute the total flux of the Ly α emission. Despite of the flux anomaly observed in image *e* of galaxy *B1* as discussed in §4.1, the effect is likely localised (since image *e* of *B2* does not show the same brightness enhancement) and therefore will not significantly bias the total Ly α flux from the extended nebula. After correcting the lensing magnification for each spaxel, we obtain a total flux of $f_{\text{Ly}\alpha}(B) = (7.4 \pm 0.2) \times 10^{-18} \text{ erg s}^{-1} \text{ cm}^{-2}$, integrated across the wavelength range of 5766–5796 Å (the same wavelength window for constructing the narrow-band image described above) and summed over all spaxels within the $3\text{-}\sigma$ contour in image *e*. At $z = 3.754$, the observed Ly α flux translates to a total luminosity of $L_{\text{Ly}\alpha}(B) = (9.8 \pm 0.2) \times 10^{41} \text{ erg s}^{-1}$.

For both systems, we also extract the de-lensed one-dimensional Ly α surface brightness profile in the source plane starting from the galaxy continuum regions to the edge of each nebula (near the $3\text{-}\sigma$ surface brightness contours), as shown in Figure 9. In §5.3 below, we derive the velocity gradient within the nebulae in both systems. As the velocity gradient suggests non-spherical gas flows in both systems, we therefore use a series of $2'' \times 0''.6$ ($1'' \times 0''.15$) pseudo slits for System *A* (System *B*), instead of circular annuli. We then extract the surface brightness profiles along directions guided by the velocity gradient within the nebulae (cyan dashed arrows in Figures 7 and 8; also see §5.3 below). The position angle of the pseudo slit is 25° north through east for System *A* and 60° north through west for System *B*. The first aperture (distance of zero) is centered on the de-lensed locations of galaxy *A1* (*A2* and *A3*) for the northern (southern) nebula in System *A*, and the distance of the subsequent apertures are measured from these corresponding continuum regions. For System *B*, the distance is measured from the location of *B1*, where we put the first aperture. We show the surface brightness profiles for System *A* both before and after including the Ly α flux inside the DLA troughs from star forming regions (see Figure 4).

As discussed above, Ly α surface brightness from the southern nebula agrees well across all three multiple images before including Ly α flux from DLA troughs, while image *a* becomes dimmer than images *b* and *c* after including the Ly α flux from the DLA troughs, suggesting a relatively smaller magnification factor in image *a* than what is predicted by the lens model at the locations of *A2a* and *A3a*. Figure 9 shows that both Systems *A* and *B* exhibit a general decline in Ly α surface brightness with increasing projected distance. Applying a simple exponential profile to characterize the observed surface brightness, $\text{SB}(\text{Ly}\alpha) \propto \exp(-D/D_s)$, we find a best-fit scale radius of $D_s \approx 18$ pkpc for System *A* and $D_s \approx 1.5$ kpc for System *B* (see Figure 9), corresponding to a half-light radius of $r_e \approx 30$ and 2.5 pkpc for Systems *A* and *B*, respectively. These are consistent with the typical size found for Lyman break galaxies (e.g. Steidel et al. 2011) and LAEs (e.g. Wisotzki et al. 2016; Leclercq et al. 2017).

At the same time, we also see a suppressed Ly α surface brightness at the locations of the galaxies. The suppression resembles what is seen in the “net absorption” sub-sample of stacked Ly α surface brightness profiles of (Steidel et al. 2011). We propose that the suppression may be attributed

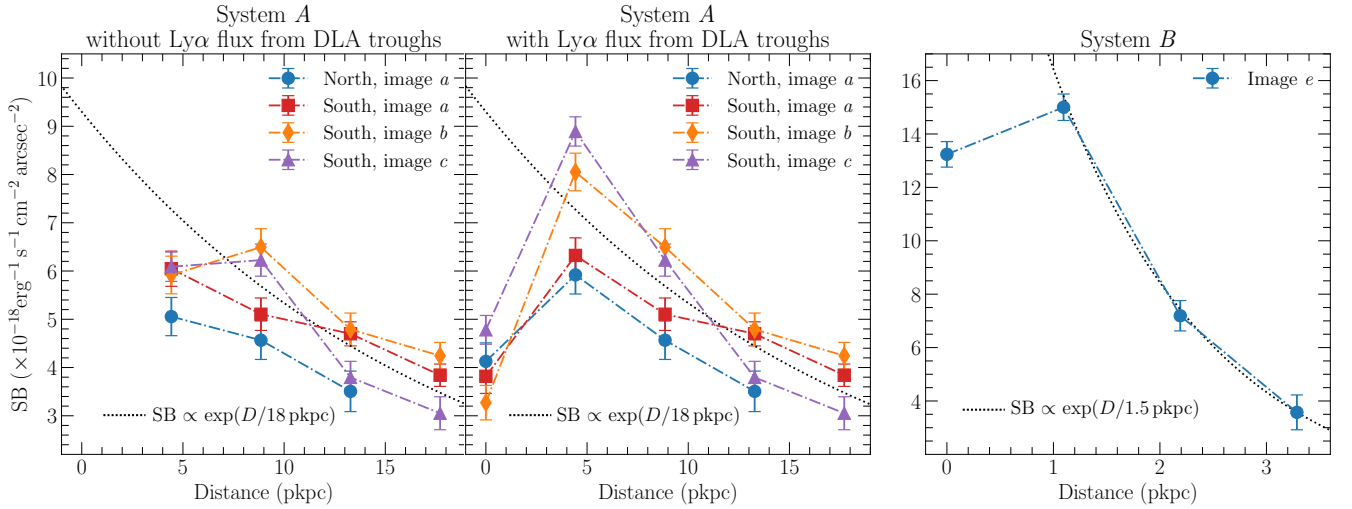


Figure 9. De-lensed $\text{Ly}\alpha$ surface brightness profile, extracted along the directions indicated in Figures 7 and 8. For System A, we present the surface brightness profile both before and after including the $\text{Ly}\alpha$ flux from the DLA troughs at the locations of galaxy continuum. Distance is measured from the location of A1 (A2 and A3) for the northern (southern) nebula. For System B, zero distance corresponds to the location of B1. Note that we use rectangle apertures to extract the surface brightness profile as guided by the velocity gradient within the nebulae, instead of circular annuli (see text). In both systems, there is a decrease in surface brightness at small distances. The suppression may be attributed to either attenuation by the observed high neutral gas column density and possibly high dust content in System A or by a reduced total gas column as a result of galactic scale outflows in System B.

to attenuation by dusty outflows, which is supported by the observed high neutral gas column density and blueshifted low-ionization ISM absorption line in System A. Under the dusty outflow scenario, the radial extent of the observed dip in the center of the $\text{Ly}\alpha$ surface brightness profile is then a direct measure of the projected radius of the dusty outflows, which in the present cases amounts to $\lesssim 5$ pkpc for System A and $\lesssim 1$ pkpc for System B. Dust in the ISM could also contribute to the suppression of the $\text{Ly}\alpha$ signal in the gap, which would imply an anisotropic distribution of the dusty material in the ISM given the presence of extended $\text{Ly}\alpha$ nebulae at larger distances away from the line-of-sight. Alternatively, the suppression may be attributed to a reduced $N(\text{HI})$ as a result of galactic scale outflows or galaxy interactions (e.g., Johnson et al. 2014).

5.2 Spatial variation of line profiles

In addition to the surface brightness variation in the narrow-band images, the $\text{Ly}\alpha$ nebulae in both systems exhibit a double-peak profile with a significantly enhanced red peak that indicates expansion/outflowing motions. In the *top-left* panel of Figure 10, we present stacked $\text{Ly}\alpha$ spectra from the northern and southern nebulae in System A. The spectra are extracted separately from within the $3\text{-}\sigma$ contours in Column (2) of Figure 6. In the *top-right* panel of Figure 10, we present stacked $\text{Ly}\alpha$ spectra for System B, extracted from within the low-surface brightness (between $3\text{-}\sigma$ and $8\text{-}\sigma$ contours) and high-surface brightness (within the $8\text{-}\sigma$ contours) regions shown in Figure 8. An overall shift in wavelength, both in the peak locations and the location of the valley of the $\text{Ly}\alpha$ line, is clearly seen between the northern and southern nebulae in System A, with the northern nebula being blueshifted by ≈ 200 km s^{-1} relative to the southern one, suggesting a large velocity gradient across the line-emitting

region. At the same time, no significant differences are seen between low- and high-surface brightness regions in System B.

To investigate in detail the velocity offset and possible spatial fluctuations in the $\text{Ly}\alpha$ profiles across both nebulae, we need to employ smaller apertures for extracting $\text{Ly}\alpha$ spectra. Specifically, we consider two competing factors when determining the extraction apertures: (1) the S/N necessary to obtain significant signal in both the blue and red peaks and (2) possible spatial smearing of the extracted $\text{Ly}\alpha$ profile over a large aperture that may lead to erroneous characteristics of the $\text{Ly}\alpha$ profile. Because of the low surface brightness nature across all regions in System A, the $\text{Ly}\alpha$ line per spaxel does not have sufficiently high signals. We therefore experiment with extracting $\text{Ly}\alpha$ spectra from a range of aperture sizes to identify an appropriate aperture size for achieving a sufficiently high S/N while limiting the smearing effect from combining different regions. We obtain the optimal extraction aperture from a localized, small area with a radius of $0''.5$ centered near the highest surface brightness peak in the reconstructed source-plane narrow-band image (blue dashed circles in Column (2) of Figure 7). We then identify the spaxels located within this area in the image plane in all three multiple images *a*, *b* and *c*, and construct a template spectrum for System A by coadding the spectra from all identified spaxels, which contains the information of gas properties in the brightest region of the nebula. The template spectrum is displayed in the *bottom-left* panel of Figure 10.

Although the S/N of the template spectrum is lower than what is seen in the large-area stacks (*upper-left* panel of Figure 10), the signal is strong enough to demonstrate the significant difference between the $\text{Ly}\alpha$ profiles extracted from small and large areas. Specifically, the template spectrum has a narrower width than the large-area stacks from

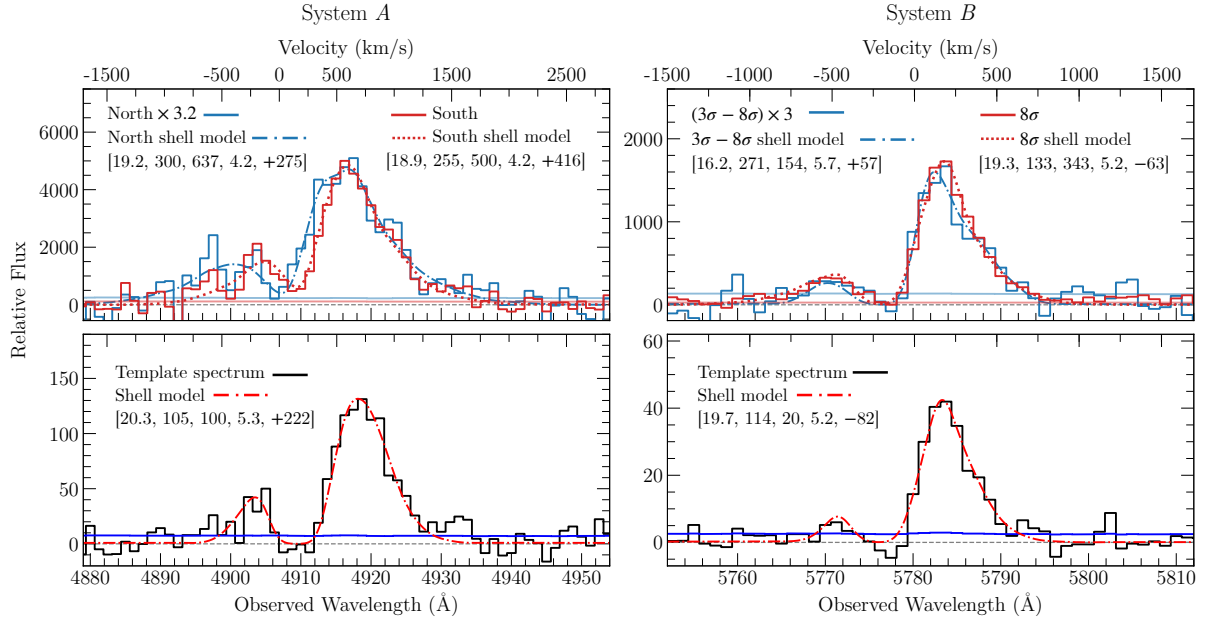


Figure 10. Spatial variation of the observed Ly α profiles and its impact on the best-fit shell model for Systems A (left) and B (right). *Top* panels display the summed Ly α line profiles over a large area, while *bottom* panels display the template Ly α profiles extracted from localized, small apertures indicated in Figure 7 for System A and stacked brightest pixels from multiple images *c*, *d* and *e* for System B (see text). The corresponding best-fit model profiles from the expanding shell model described in the text are included as dotted and dash-dotted curves with the best-fit parameters summarized in the legend, following the order of $[\log N(\text{HI})/\text{cm}^{-2}, v_{\text{exp}} (\text{km s}^{-1}), \sigma_i (\text{km s}^{-1}), \log T_{\text{eff}}/\text{K}, \Delta v (\text{km s}^{-1})]$. For the large area sums in the *top* panels, System A is naturally divided into northern and southern nebulae, while System B is broadly divided by low- and high-surface brightness regions, between within and outside of the $8\text{-}\sigma$ contours. Zero velocity corresponds to $z_{\text{sys}} = 3.0364$ for System A, which is the systemic redshift of A1, and $z_{\text{sys}} = 3.7540$ for System B, which is the systemic redshift of B1 and B2. The largest distinction between large and small aperture stacks is seen in System A, both in terms of the flux level in the valley between the blue and red peak as well as the profile line width, which is captured by a combination of neutral hydrogen column density $\log N(\text{HI})/\text{cm}^{-2}$, intrinsic line width (σ_i) and effective temperature ($\log T_{\text{eff}}/\text{K}$). The line profiles are significantly broader in the stacked spectra obtained over a larger area. In contrast, such distinction is much less visible in System B.

both the northern and southern nebulae. In addition, the template spectrum exhibit a flux level that is consistent with zero at the bottom of the valley between the red and blue peaks. The observed zero flux in the valley is consistently seen across the nebulae in all spectra extracted from small apertures, and differs from the distinctly non-zero flux observed in the stacked spectra over the larger nebulae (see also Figure 3 of Caminha et al. 2017). Such difference can be naturally explained by the presence of a large velocity gradient in the nebulae that results in smearing of the combined Ly α profile. But because a non-zero flux in the valley of a double-peak Ly α profile would lead to very different parameters constraints for the expanding shell model (e.g. Dijkstra et al. 2006; Verhamme et al. 2006; Hansen & Oh 2006; Laursen et al. 2009; Schaerer et al. 2011; Gronke et al. 2015, also see below), the ability to spatially resolve the velocity field is necessary for obtaining accurate constraints for the underlying gas properties. In our study, we leverage lensing magnifications to resolve spatial variations on scales as small as ≈ 2 pkpc along both nebulae (Systems A and B) in ground-based, seeing-limited data, though we caution that variations on smaller scales may still be present in these clouds (e.g. Cantalupo et al. 2019).

For System B, because the nebula is significantly brighter than what is seen in System A and the distinction in the observed Ly α profile is subtle between different locations, we construct a template spectrum using only

the brightest pixels in images *c*, *d* and *e* (one pixel from each image) to better constrain possible velocity gradient and spatial variation over a small area. The locations of the three brightest pixels included in the template spectrum are indicated by the black arrows in Column (1) of Figure 8. The template spectrum for System B is displayed in the *bottom-right* panel of Figure 10, and does not show significant differences from the stacked spectra from larger areas (*upper-right* panel of Figure 10).

5.3 Physical properties of Ly α nebulae under an expanding shell model

We utilize the spatially and spectrally resolved Ly α profiles from MUSE observations and a Ly α Monte Carlo radiative transfer code `tlac` (Gronke & Dijkstra 2014; Gronke et al. 2015) to model the physical properties of the line-emitting gas. We adopt an expanding shell model that has successfully explained many observed Ly α spectra across a wide range of redshifts based on a finite set of parameters, including the neutral hydrogen column density, $N(\text{H I})$, the expansion velocity, v_{exp} , intrinsic line width, σ_i , effective temperature, T_{eff} , and systemic velocity, Δv (e.g. Verhamme et al. 2006; Yang et al. 2017; Gronke 2017).

As illustrated in Verhamme et al. (2006), while there are considerable degeneracies between different parameters of the shell model, the peak separation increases primarily

Table 6. Summary of the best-fit parameters (95% confidence interval) for characterizing the observed Ly α profile under an expanding shell model.

System A, $z_{\text{sys}} = 3.0364$						
Spectrum	$\log N(\text{HI})/\text{cm}^{-2}$	v_{exp} (km/s)	σ_i^a (km/s)	$\log T_{\text{eff}}/\text{K}$	Δv^b (km/s)	χ^2_ν
North	$19.2^{+0.2}_{-0.3}$	300^{+40}_{-30}	637^{+28}_{-51}	$4.2^{+0.6}_{-1.2}$	275^{+60}_{-37}	6.6
South	$18.9^{+0.2}_{-0.1}$	255^{+6}_{-36}	500^{+49}_{-7}	$4.2^{+0.1}_{-0.5}$	416^{+7}_{-44}	10.6
Template spectrum	$20.3^{+0.2}_{-0.2}$	105^{+27}_{-20}	100	$5.3^{+0.2}_{-0.2}$	222^{+22}_{-30}	2.4
System B, $z_{\text{sys}} = 3.7540$						
$3\sigma - 8\sigma$	$16.2^{+3.4}_{-0.7}$	271^{+63}_{-174}	154^{+218}_{-57}	$5.7^{+0.2}_{-2.4}$	57^{+57}_{-138}	0.9
8σ	$19.3^{+0.2}_{-0.1}$	133^{+10}_{-15}	343^{+20}_{-22}	$5.2^{+0.0}_{-0.2}$	-63^{+13}_{-19}	5.3
Template spectrum	$19.7^{+0.1}_{-0.2}$	114^{+17}_{-19}	20	$5.2^{+0.2}_{-0.2}$	-82^{+25}_{-19}	1.3

^a Values without errors indicate a prior specified by the nebular emission lines (see Table 5).

^b Relative velocity with respect to z_{sys} .

with $N(\text{HI})$, and the red-to-blue peak ratio increases with v_{exp} , while T_{eff} and σ_i set the overall line width (see also Gronke et al. 2015, for a more detailed discussion on the effect of these parameters). In most cases this simple shell model provides a crude estimate of the underlying kinematic properties of the gas, but there are also known cases where the model failed to provide a good fit to data (e.g. Kulas et al. 2012; Orlitová et al. 2018).

We note that the shell models are developed for a spherical shell expanding radially outward, which may work better for unresolved Ly α nebulae under the assumption that the emission sources are at the center of the gas. In applying these models to System A, for which the Ly α photons may originate outside of the nebulae, we attribute the enhanced red peak in the observed Ly α profile per spaxel to cloud expansion relative to a fiducial reference point interior to the cloud along the observer’s line of sight. In addition, we attribute the observed velocity shear to the motion of this reference point relative to the systemic redshift of the galaxies. Although the source of photons likely lies outside of the nebulae (see §6 below for discussions on the origin of Ly α photons), the problem is equivalent to extracting the Ly α signal from one hemisphere of a spherical shell. Because of spherical isotropy inherent to the shell model, we expect that considering one hemisphere would result in an overall reduction in the amplitude of the signal, instead of altering the line profile. Guided by this understanding, we proceed with approximating the signal in each spaxel with expectations from an expanding shell model for constraining the systemic velocity at each location.

For our analysis, we assume a homogeneous medium of constant gas density and compare the observed Ly α profiles with predictions over a grid of model parameters. To fully explore the allowed parameter space, we construct a model grid that covers $\log N(\text{HI})/\text{cm}^{-2}$ from 15.1 to 21.1, v_{exp} from 10 to 400 km s^{-1} , σ_i from 25 to 700 km s^{-1} , $\log T_{\text{eff}}/\text{K}$ from 3.0 to 6.0, and Δv from -100 to 550 km s^{-1} . The velocity offset, Δv , is calculated with respect to the systemic redshift z_{sys} listed in Table 6. We use 10,000 photons and 100 frequency bins to generate each model profile. Each model profile is also convolved with MUSE line spread function be-

fore compared to observations. Given the uncertainty of the dust attenuation effect on Ly α photons, we do not include dust in our models and it will be explored separately in the future. For each model, we compute a likelihood function \mathcal{L} defined as

$$\begin{aligned} \mathcal{L}(N_{\text{HI}}, v_{\text{exp}}, \sigma_i, T_{\text{eff}}, \Delta v) \\ = \prod_j \exp \left\{ - \frac{[D(\lambda_j) - M(\lambda_j | N_{\text{HI}}, v_{\text{exp}}, \sigma_i, T_{\text{eff}}, \Delta v)]^2}{2 S^2(\lambda_j)} \right\}, \end{aligned} \quad (6)$$

where $D(\lambda_j)$ and $M(\lambda_j)$ are the observed and model spectra, respectively, and $S(\lambda_j)$ is the corresponding error spectrum. The likelihood function is computed over the wavelength range of 4890-4930 Å (5766-5796 Å) for System A (System B), and can be translated to χ^2 following $\chi^2 = -2 \ln \mathcal{L}$. We then construct a marginalised likelihood function for each parameter by integrating \mathcal{L} over all other parameters, and find the 95% confidence interval centered around the best-fit value. Note that since we do not explicitly include turbulent broadening in the models here, the temperature inferred from the model represents an effective temperature that includes non-thermal motion. For reference, for an intrinsic gas temperature of $T = 10^4$ K, an inferred effective temperature of $T_{\text{eff}} = 10^5$ (10^6) K implies an underlying bulk flow of $\sigma_v^{\text{bulk}} \approx 30$ (90) km s^{-1} .

To illustrate the impact of velocity smearing on the Ly α profile analysis, we first consider stacked spectra obtained over a large area along with the best-fit model profiles (*top* panels of Figure 10). The best-fit parameters and the associated 95% confidence intervals are presented in Table 6. The large χ^2_ν values in Table 6 show that an expanding shell model fails to provide a good fit for the high S/N stacked Ly α spectra for both systems. A close examination of the profiles in the *top* panels of Figure 10 shows that the best-fit models with an uncharacteristically large intrinsic line width of $\sigma_i \approx 500$ -650 km s^{-1} provide a poor fit to the blue peak of the northern and southern nebulae in System A. The best-fit σ_i is substantially broader than either what is seen in the nebular emission lines (see Table 5) or what is expected for the velocity dispersion in halos of a comparable mass scale for the host galaxies (e.g. $M_{\text{halo}} < 10^{12} M_\odot$;

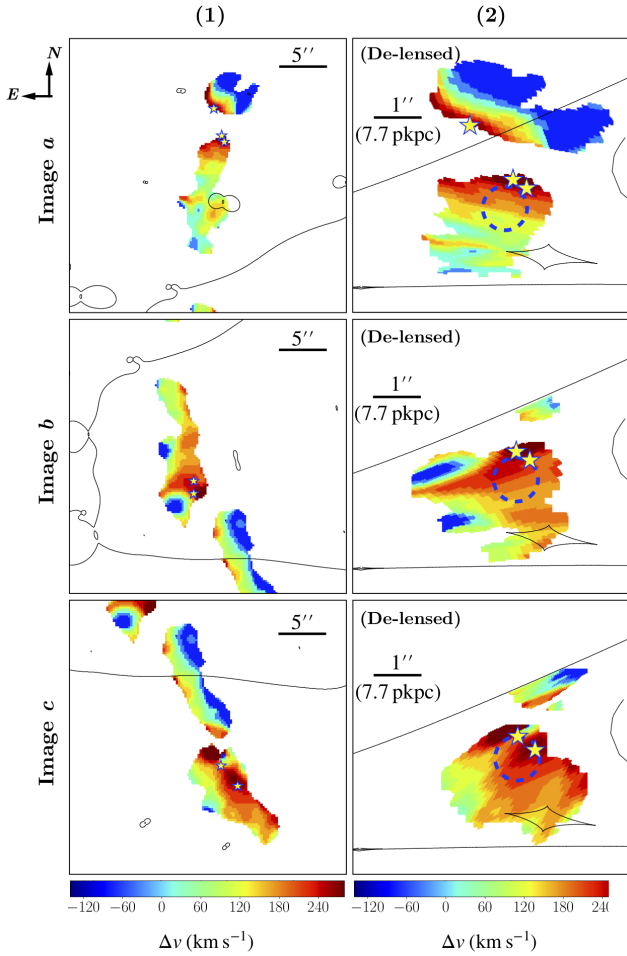


Figure 11. Column (1): velocity map of multiple images *a*, *b* and *c* in System *A*, derived from cross-correlating the best-fit shell model for the template spectrum (*bottom-left* panel of Figure 10) and spectra extracted from spaxels within the $3\text{-}\sigma$ contours. Zero velocity corresponds to $z_{\text{sys}} = 3.0364$, which is the systemic redshift of *A1* derived from nebular emission lines. Column (2): de-lensed velocity map of individual images in the source plane. Star symbols mark the positions of the associated star-forming galaxies identified in *HST* images (see Figures 6 and 7). The blue dashed circles, same as in Column (2) of Figure 7, mark the apertures for the template spectrum extraction, which we use for the shell model analysis.

Trainor & Steidel 2012). For System *B*, while the small χ^2_ν for the stacked spectrum from low-surface brightness regions suggests a good fit to the data, the model remains poorly constrained with large associated uncertainties due to the low S/N of the data. At the same time, the best-fit shell model produces a relatively poor fit to the blue peak of high S/N , high-surface brightness regions, leading to a large χ^2_ν .

To improve the precision and accuracy of the model constraints, we perform the profile analysis for the template spectra extracted from localized, small apertures presented in the *bottom* panels of Figure 10. In addition, we adopt the observed nebular line width (see Table 5) as a prior for modelling the Ly α profiles. This is justified by the understanding that these Ly α photons likely originate in the star-forming regions of the associated galaxies (see §6 below). Specifically, we set $\sigma_i = 100 \text{ km s}^{-1}$ for System *A* based on the observed

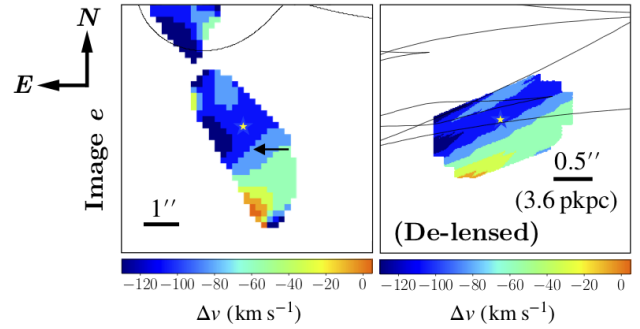


Figure 12. *Left*: velocity map of image *e* in System *B*, derived from cross-correlating the best-fit shell model for the template spectrum (*bottom-right* panel of Figure 10) and spectra extracted from spaxels within the $3\text{-}\sigma$ contour. Zero velocity corresponds to $z_{\text{sys}} = 3.7540$, which is the systemic redshift of *B1/B2* derived from nebular emission lines. *Right*: de-lensed velocity map of image *e* in the source plane. Star symbols mark the position of *B1/B2* determined from *HST* images (see Figure 8). The black arrow, same as in Column (1) of Figure 8, indicate the brightest pixel in image *e* that is included in the template spectrum.

FWHM of $\approx 240 \text{ km s}^{-1}$ in galaxy *A2*, and $\sigma_i = 20 \text{ km s}^{-1}$ for System *B* based on the observed FWHM of $\approx 40 \text{ km s}^{-1}$ in galaxies *B1/B2*. The best-fit model profiles are shown in dotted and dash-dotted curves and best-fit parameters are presented in Table 6. It is immediately clear that the resulting χ^2_ν is reduced substantially and the parameters are well-constrained. In contrast, setting the same prior on σ_i when fitting the stacked spectra from larger apertures results in poor model fits with larger χ^2_ν values (see Appendix). This again underscores the smearing effect on stacked Ly α profiles extracted from larger areas, which can significantly bias the constrained gas properties with the presence of velocity gradient and spatial variations in the line emitting region. The best-fit models also suggest that both Systems *A* and *B* consistently require a large neutral hydrogen column density, $\log N(\text{H I})/\text{cm}^{-2} \gtrsim 19$ for explaining the observed Ly α profiles from localized locations.

Because of the competing factors between spectral qualities (i.e., S/N) and velocity smearing, in addition to a strong degeneracy between different model parameters with modest S/N data, we continue the analysis with a focus on constraining the velocity field, Δv , across the Ly α nebulae. This is achieved by cross-correlating the best-fit shell model for the template Ly α spectra with each spaxel within the $3\text{-}\sigma$ contours in both systems to measure velocity offsets at different locations. To optimize the cross-correlation analysis, we spatially smooth the data cube with a Gaussian filter of $\text{FWHM}_{\text{smooth}} = 1''$ before extracting individual spectra. The resulting velocity maps are presented in Figure 11 for System *A* and Figure 12 for System *B*. We also present de-lensed velocity maps of both nebulae in the source plane. We have also experimented with constraining the velocity gradient by fitting an asymmetric Gaussian function (e.g., see Eq.1 of Leclercq et al. 2020) to the red peak of the Ly α profile from every spaxel within the $3\text{-}\sigma$ contour in both systems, and we obtain a similar velocity gradient as shown in Figures 11 and 12. Our method utilising the best-fit model of the template spectra enables us to determine the systemic velocity offset Δv of the line-emitting gas in the frame of the

nearby star-forming region, thereby connecting the nebulae with the associated star-forming regions.

Our analysis of System *A* has uncovered a highly organized velocity field across the Ly α emitting nebulae, with increasing velocity offset from $\Delta v \approx 0 \text{ km s}^{-1}$ at $\approx 11 \text{ pkpc}$ south of galaxies *A2* and *A3* to $\Delta v \approx +250 \text{ km s}^{-1}$ at the locations of these galaxies (Figure 11). In the north, the velocity offset decreases from $\Delta v \gtrsim +200 \text{ km s}^{-1}$ at the location of galaxy *A1* to $\Delta v \approx -150 \text{ km s}^{-1}$ at $\approx 13 \text{ pkpc}$ northwest of *A1*. The inferred velocity offset shows that the line-emitting gas closest to the galaxies is receding from the galaxies. Different from the extended blue wings seen in ISM absorption lines, this velocity offset seen in Ly α emission places the gas behind the star-forming region. The observed steep velocity gradient, $|\Delta v / \Delta r_{\perp}| \approx 22\text{--}27 \text{ km s}^{-1} \text{ pkpc}^{-1}$, together with a large best-fit $N(\text{H I})$ and an enhanced red peak in the Ly α profile across the nebula supports a scenario in which high column density gas is driven outward from the galaxies to beyond 10 pkpc in projected distance into the low-density surroundings. Due to a lack of AGN activities (see §4.4), the outflows are likely driven by star formation in these young galaxies.

It is interesting that there exists an apparent gap in Ly α signal between the northern and southern nebulae. One possible explanation for this gap is a reduced $N(\text{H I})$ as a result of galaxy interactions. A lack of strong Ly α absorber has been seen at projected distances of $< 20 \text{ pkpc}$ from an interacting galaxy pair at low redshift with an upper limit of $\log N(\text{H I})/\text{cm}^{-2} \lesssim 13.7$ (e.g. Johnson et al. 2014). In the optically thin regime, we estimate a $2\text{-}\sigma$ upper limit of $\log N(\text{H I})/\text{cm}^{-2} < 16.4$ at $\approx 5 \text{ pkpc}$ based on the observed $2\text{-}\sigma$ upper limit in Ly α surface brightness and an assumption of 100% escape fraction of ionizing photons from the galaxies. While at this limit, the gas would still be optically thick to Ly α photons, we cannot rule out the possibility of a significantly lower $N(\text{H I})$. Other plausible explanations for the gap also include a lack of illumination from young stars due to anisotropic leakage of Ly α and ionizing photons, and attenuation of Ly α signal due to highly neutral, dusty gas in-between these galaxies (also see discussion in §6 below).

In contrast, System *B* exhibits distinct properties from System *A*. The Ly α nebula appears to be distributed symmetrically around galaxies *B1* and *B2* with the peak intensity located close to star forming regions. The inferred line-of-sight velocity offset of $\approx -100 \text{ km s}^{-1}$ near the location of the galaxies, coupled with the observed Ly α profile, again supports an outflow scenario from the galaxies. The observed velocity gradient of $|\Delta v / \Delta r_{\perp}| \approx 20 \text{ km s}^{-1} \text{ kpc}^{-1}$ toward the outer edge of the nebula may be explained by a line-of-sight projection effect.

6 DISCUSSION

We have shown that by accounting for spatial variations in the observed Ly α line profiles, we are able to determine the velocity field and constrain gas flows across the nebulae. Given the proximity of the line-emitting gas to star-forming galaxies and the relatively small velocity offset between gas and galaxies, we argue that the gas is being driven out of the star-forming regions at a modest speed. Specifically, the Ly α nebula of System *B* exhibits a relatively symmetrical

morphology with the peak of the Ly α emission located close to the star-forming regions. This configuration is typical of low-mass LAEs at high redshifts (e.g. Wisotzki et al. 2016; Leclercq et al. 2017), and suggests that gas flows outward from the star-forming regions into the low-density halo environment. At the same time, galaxies *A1*, *A2* and *A3* share similar spectral and photometric properties (see §4). The close proximity of these three galaxies suggest that they may share an interactive group environment and are part of a common CGM. The Ly α nebulae are clearly offset to one side of the galaxies with the highest surface brightness regions bordering the continuum-emitting regions (see Figures 6 and 7). While the star-forming regions contribute significantly to the extended Ly α emission, the connection between the star-forming regions and the large-scale outflows remains uncertain.

We consider two plausible scenarios for the origin of the outflows. First, the northern nebula originates in gas flowing out of *A1*, while the southern nebula originates in gas flowing out of galaxies *A2* and *A3*. This is plausible if all three galaxies are capable of driving galactic scale superwinds. Applying the conversion factor of Madau & Dickinson (2014), we estimate an unobscured SFR of ≈ 22 , 5 and $4 M_{\odot} \text{ yr}^{-1}$ for galaxies *A1*, *A2*, and *A3*, respectively, based on the observed rest-frame UV absolute magnitudes M_{1500} presented in Table 2. In the presence of dust, this observed M_{1500} and inferred SFR are likely lower limits to the intrinsic values. In addition, we estimate a total projected area based on the continuum regions determined by SExtractor (see §4.1) and apply lensing magnification corrections based on the fine-tuned lens model (see §3). We find the intrinsic projected area of *A1*, *A2*, and *A3* to be ≈ 50 , 11 and 11 pkpc^2 , respectively. For galaxies *A2* and *A3*, these are based on an average over all three images, *a*, *b*, and *c* after lensing magnification corrections. Combining the estimated unobscured SFR and projected area leads to an estimate of SFR per unit area of $\gtrsim 0.4 M_{\odot} \text{ yr}^{-1} \text{ pkpc}^{-2}$ in these individual galaxies. This exceeds the empirical threshold seen in driving galactic scale superwinds in local starburst galaxies (e.g. Heckman et al. 2015).

Alternatively, galaxy *A1* may be the single dominant source driving the outflows seen in both the northern and southern nebulae. Apart from being the most massive galaxy with the highest SFR in the group, *A1* also shows more extended blue wings in the low-ionization ISM absorption lines (see Figure 4 and Table ??), suggesting the presence of galactic outflows that are more prominent than what is seen from the same line features in galaxies *A2* and *A3*. In this scenario where galaxy *A1* is the origin of the outflows on both sides, the gap in Ly α emission between the northern and southern nebulae is likely due to dusty outflow materials from galaxy *A1* that cover the gap area along the line-of-sight.

A remaining question of the observed line-emitting nebulae is the origin of Ly α photons. As described earlier, multiple mechanisms can lead to Ly α emission in diffuse gas, including cooling radiation, fluorescence powered by ionizing photons from either star-forming regions or AGN, and resonant scattering by neutral hydrogen gas (e.g., Hogan & Weymann 1987; Gould & Weinberg 1996; Cantalupo et al. 2005; Kollmeier et al. 2010; Faucher-Giguère et al. 2010; Hennawi & Prochaska 2013). Disentangling between differ-

ent mechanisms that are responsible for the observed Ly α signals is challenging, especially when the Ly α line is the only observable feature in the nebulae.

For the two systems in our study, however, the observed spectral properties of the Ly α line enable us to rule out cooling radiation and photo-ionization due to the cosmic UV background radiation as a dominant mechanism for powering the observed emission. Specifically, radiatively cooled gas is expected to condense and sink through the hot ambient medium, resulting in infall, and the majority of the photons will travel through the infalling clouds before escaping the medium (e.g., Faucher-Giguère et al. 2010). The expectation of an enhanced blue-peak from infalling gas is inconsistent with the observations. In addition, the expected Ly α fluorescence signal from cosmic UV background alone is low with surface brightness of $\lesssim 10^{-19}$ erg s $^{-1}$ cm $^{-2}$ arcsec $^{-2}$ (e.g., Kollmeier et al. 2010).

We therefore proceed with considerations of the two remaining scenarios: (1) Ly α photons arising as a result of fluorescence powered by ionizing photons from star-forming regions and (2) Ly α photons produced in the galaxies and resonantly scattered by neutral hydrogen in the nebulae. The first scenario requires a non-zero escape fraction of ionizing photons from the galaxies, while the second scenario corresponds to the shell model analysis described in §5.3. Here we also discuss the implications of these scenarios.

6.1 Ly α emission from recombination radiation and implications for the escape fraction of ionizing radiation from star-forming galaxies

We first consider the possibility that the observed Ly α signals are powered by *in situ* star formation directly underneath the nebulae. Available deep *HST* F606W image places strong constraints on the rest-frame UV continuum flux at the location of the nebulae. Using the integrated Ly α luminosity of $L_{\text{Ly}\alpha} = (2.15 \pm 0.07) \times 10^{42}$ erg s $^{-1}$ ($[3.49 \pm 0.08] \times 10^{42}$ erg s $^{-1}$) for the northern (southern) nebula of System *A*, we infer an SFR of ≈ 1.1 (2.3) M $_{\odot}$ yr $^{-1}$ based on a conversion factor of Ly α /H α = 8.7 (Hayes 2015, and references therein) and the H α -SFR relation of Kennicutt & Evans (2012). From the inferred SFR, we derive the expected apparent magnitude in the F606W bandpass (corresponding to 1500 Å in the rest frame at $z \approx 3$) of $AB(\text{F606W}) \approx 27.3$ (26.5) using the FUV flux-SFR relation of Madau & Dickinson (2014) for the underlying star-forming regions in the northern (southern) nebula. The inferred F606W magnitude is roughly more than two magnitudes brighter than the 2- σ detection limit in the F606W bandpass ($AB(\text{F606W}) \approx 29$ within an aperture of 0''.5 in diameter), but no flux is detected at the location of the nebulae away from the galaxies. While we consider *in situ* star formation an unlikely scenario for powering the Ly α signals, we cannot rule out the possibility that dust obscurations may have played a role in blocking the FUV photons along the line of sight. Deeper imaging data at submillimeter are needed for constraining the effect of dust. In the following discussion, we proceed with considerations of external sources for powering the observed Ly α signals.

For photo-ionization by the nearby galaxies, the observed Ly α intensity is connected to the incident ionizing radiation field and the discussion often involves consider-

ations of two different regimes, optically thin versus optically thick gas. For the purpose of our study, both Systems *A* and *B* consistently require a large $N(\text{H I})$, exceeding $\log N(\text{H I})/\text{cm}^{-2} \approx 19$ (Table 6), for explaining the observed Ly α profile. We therefore consider only optically-thick regime in the subsequent discussion.

In optically-thick regime, ionization occurs in the surface of a cloud illuminated by the ionizing source and roughly 66% of all ionizing photons are converted into Ly α photons through recombination cascades in the surface layer (i.e., $\eta_{\text{B}} = 0.66$) (Osterbrock & Ferland 2006). The surface brightness of Ly α emission is connected to ionizing photon flux according to

$$\begin{aligned} \text{SB}_{\text{Ly}\alpha} &= f_g f_{\text{esc}} \frac{\eta_{\text{B}} h \nu_{\text{Ly}\alpha}}{(1+z)^4 \pi} \Phi \\ &= 3.2 \times 10^{-18} f_g f_{\text{esc}} \left(\frac{1+z}{4.0} \right)^{-4} \left(\frac{D}{10 \text{ pkpc}} \right)^{-2} \\ &\quad \left(\frac{\Phi_0}{10^7 \text{ s}^{-1} \text{ cm}^{-2}} \right) \text{ erg s}^{-1} \text{ cm}^{-2} \text{ arcsec}^{-2} \quad (7) \end{aligned}$$

where f_g is the geometric correction coefficient to account for partial illumination of the nebula and redistribution of Ly α photons, f_{esc} is the fraction of ionizing photons that escape the galaxies, D is the distance of the cloud from the ionizing source, and Φ_0 is the ionizing photon flux at a distance of 1 kpc from the source. In principle, comparing the observed Ly α surface brightness with the expected ionizing radiation field from the SED analysis of the galaxies constrains f_g and f_{esc} based on Eq. 7. In practice, uncertainties in the inferred galaxy spectra are large. Therefore, it is not trivial to obtain accurate constraints for f_g and f_{esc} .

For System *A*, we estimate the total ionizing photon fluxes from *A1*, *A2* and *A3* using the best-fit BAGPIPES model spectra and find respectively $\Phi_0 \approx 3.4 \times 10^8$, 8.1×10^7 , 5.1×10^7 s $^{-1}$ cm $^{-2}$ at $D = 10$ pkpc. Assuming $f_g = 0.5$ from numerical simulations (e.g., Cantalupo et al. 2005; Kollmeier et al. 2010) and $f_{\text{esc}} < 10\%$ as a fiducial upper limit for ionizing photon escape fraction (e.g. Chen et al. 2007; Vanzella et al. 2010; Grazian et al. 2017), the observed peak Ly α surface brightness of 7.3×10^{-18} erg s $^{-1}$ cm $^{-2}$ arcsec $^{-2}$ (the 6- σ contour in Figure 7) implies a distance limit of $D < 8.5$ pkpc from *A1* and $D < 3.3$ pkpc from *A3*. Adopting the low-intensity contour of 3.7×10^{-18} erg s $^{-1}$ cm $^{-2}$ arcsec $^{-2}$ would increase the distance limit by 40% to $D < 12$ pkpc from *A1* and $D < 4.6$ pkpc from *A3*. The observed extent of Ly α emission of $\gtrsim 10$ pkpc (see Figure 7) therefore requires *A1* to be the dominant source of ionizing photons with an escape fraction $\sim 10\%$. Current observations suggest that the escape fraction of ionizing photons from massive ($>L_*$) galaxies at $z \approx 3$ is much smaller than 10% (e.g. Grazian et al. 2017). The inferred large $\log(\text{H I})$ based on Ly α line profiles also suggests that f_{esc} is likely to be small. In addition, in §6.2 below, we show that resonant scattering of Ly α photons produced in the star-forming regions can account for the full extent of the Ly α nebulae. We therefore conclude that recombination radiation from photo-ionized gas alone is unlikely to dominate the observed Ly α signal in System *A*.

We repeat the same exercise for System *B*. Due to the smaller physical scale of System *B*, we estimate the ionizing photon flux at a distance of $D = 1$ pkpc. Using the

best-fit BAGPIPES model spectra, we obtain the total ionizing photon flux from *B1* and *B2* combined to be $\Phi \approx 1.4 \times 10^8 \text{ s}^{-1} \text{ cm}^{-2}$ at 1 pkpc. The observed surface brightness of $7.5 \times 10^{-18} \text{ erg s}^{-1} \text{ cm}^{-2} \text{ arcsec}^{-2}$ (the $8\text{-}\sigma$ contour in Figure 8) leads to $(f_{\text{g}} f_{\text{esc}}) \approx 33\%$, or $f_{\text{esc}} = 66\%$ assuming $f_{\text{g}} = 0.5$. At the limit of $f_{\text{esc}} < 1$, we infer the distance limit of $D < 1.2$ pkpc for the high-intensity contours. With the low-intensity surface brightness of $2.8 \times 10^{-18} \text{ erg s}^{-1} \text{ cm}^{-2} \text{ arcsec}^{-2}$ (the $3\text{-}\sigma$ contour in Figure 8), the inferred distance limit is increased to $D < 2$ pkpc. Because the observed Ly α emission extends to $\gtrsim 4$ pkpc in the source plane (see Figure 8), we conclude that recombination radiation from photo-ionized gas alone *cannot* explain all of the observed Ly α photons away from the galaxies in System *B*.

6.2 Ly α emission from scattering and implications for dust attenuation

Given the star-forming nature of the galaxies in both Systems *A* and *B*, we now consider the scenario in which the Ly α photons are produced in the star-forming ISM of the galaxies and resonantly scattered through the spatially extended nebulae. Using the estimated SFR in the 16%–84% confidence interval for galaxies *A1*, *A2* and *A3* (see Table 4), we infer a total intrinsic Ly α luminosity of $L_{\text{Ly}\alpha}^{\text{int}} / (10^{44} \text{ erg s}^{-1}) = 1.46\text{--}1.65$, $0.17\text{--}0.19$, and $0.21\text{--}0.26$ for galaxies *A1*, *A2*, and *A3*, respectively, using the conversion factor of Ly α /H α = 8.7 (Hayes 2015, and references therein) and the H α -SFR relation of Kennicutt & Evans (2012). For System *B*, the same exercise leads to an intrinsic Ly α luminosity of $L_{\text{Ly}\alpha}^{\text{int}} = (1.2\text{--}2.1) \times 10^{42} \text{ erg s}^{-1}$ for galaxies *B1* and *B2* combined.

While these star-forming galaxies may be intrinsically luminous in Ly α , we expect that a large fraction of these Ly α photons are unable to escape the ISM due to a substantial amount of dust attenuation. We obtain an empirical estimate of the attenuation factor $k_{\text{dust}} = 1 - L_{\text{Ly}\alpha}^{\text{obs}} / L_{\text{Ly}\alpha}^{\text{int}}$ based on the observed Ly α luminosity of $2.15 \times 10^{42} \text{ erg s}^{-1}$ for the northern nebula and $3.43 \times 10^{42} \text{ erg s}^{-1}$ for the southern nebula, and the intrinsic Ly α luminosity from star-forming regions described above. Attributing the Ly α emission of the northern (southern) nebula to the scattering of Ly α photons from galaxy *A1* (galaxies *A2* and *A3*), we estimate k_{dust} to be $\approx 98\%$ and $\approx 92\%$ for the northern and southern nebula, respectively.

Following the optically-thick prescription from Equation 7 and replacing ionizing photon flux with Ly α photon flux $\Phi_{\text{Ly}\alpha}$, we can now connect the Ly α scattering surface brightness to $L_{\text{Ly}\alpha}^{\text{int}}$ following

$$\begin{aligned} \text{SB}_{\text{Ly}\alpha} &= \frac{h \nu_{\text{Ly}\alpha} \Phi_{\text{Ly}\alpha}}{(1+z)^4 \pi} \\ &= \frac{h \nu_{\text{Ly}\alpha} (1 - k_{\text{dust}}) L_{\text{Ly}\alpha}^{\text{int}}}{(1+z)^4 4\pi^2 D^2 h \nu_{\text{Ly}\alpha}} \\ &= 2.4 \times 10^{-18} \left(\frac{1+z}{4.0} \right)^{-4} \left(\frac{D}{10 \text{ pkpc}} \right)^{-2} \\ &\quad \frac{(1 - k_{\text{dust}}) L_{\text{Ly}\alpha}^{\text{int}}}{10^{42} \text{ erg s}^{-1}} \text{ erg s}^{-1} \text{ cm}^{-2} \text{ arcsec}^{-2}. \end{aligned} \quad (8)$$

Eq. 8 leads to a distance estimate of $D_{\text{north}} \approx 14$ pkpc between the northern nebula and galaxy *A1* for an observed Ly α surface brightness of $3.7 \times 10^{-18} \text{ erg s}^{-1} \text{ cm}^{-2} \text{ arcsec}^{-2}$

(the $3\text{-}\sigma$ contour in Figure 7), an intrinsic Ly α luminosity of $L_{\text{Ly}\alpha}^{\text{int}} = (1.46\text{--}1.65) \times 10^{44} \text{ erg s}^{-1}$ for *A1*, and an attenuation factor of 98%. At higher intensity of $7.3 \times 10^{-18} \text{ erg s}^{-1} \text{ cm}^{-2} \text{ arcsec}^{-2}$ (the $6\text{-}\sigma$ contour in Figure 7), the distance is reduced to ≈ 10 pkpc. The inferred distance range is fully consistent with the extent of the northern nebula relative to *A1*. In addition, the estimated amount of dust attenuation agrees with $A_V \approx 0.7$ mag inferred from the SED analysis presented in §4.2 (see also Table 4). Based on the Calzetti et al. (2000) extinction law for starburst galaxies, the estimated stellar extinction of $A_V \approx 0.7$ mag corresponds to an extinction magnitude of $A_{1215} \approx 5.2$ mag for the Ly α emission line, or $k_{\text{dust}} \approx 99\%$ for the Ly α photons. It suggests that resonant scattering alone can fully account for the observed Ly α brightness in the northern nebula.

For the southern nebula, galaxies *A2* and *A3* together contribute to a total intrinsic Ly α luminosity of $L_{\text{Ly}\alpha}^{\text{int}} = 3.8\text{--}4.5 \times 10^{43} \text{ erg s}^{-1}$. Adopting $k_{\text{dust}} = 92\%$ leads to a distance estimate of $D_{\text{south}} \approx 10$ pkpc for the high-intensity region and $D_{\text{south}} \approx 15$ pkpc for the low-intensity region between galaxies *A2/A3* and the southern nebula. Similarly, the estimated size is consistent with the observed extent of the southern nebula (see §5.1). Although the dust attenuation of 92% is in tension with the estimated $k_{\text{dust}} \approx 99\%$ based on the SED analysis, we argue that a possible contribution of Ly α photons from galaxy *A1*, together with uncertainties in f_{esc} (see §6.1) and k_{dust} in an inhomogeneous, clumpy medium could account for the observed extent of Ly α signals in the southern nebula (e.g., Neufeld 1991; Hansen & Oh 2006).

For galaxies *B1* and *B2*, the uncertainty in $k_{\text{dust}} = 1 - L_{\text{Ly}\alpha}^{\text{obs}} / L_{\text{Ly}\alpha}^{\text{int}}$ is larger, ranging between $\approx 20\text{--}50\%$. Meanwhile, uncertainties in A_V are also larger, ranging between $A_V \approx 0.05\text{--}0.25$ for *B1* and $A_V \approx 0.5\text{--}0.7$ for *B2* (see Table 4), corresponding to a wide range of dust attenuation of $\approx 30\text{--}99\%$ for Ly α photons, in agreement with the empirical k_{dust} of $\approx 20\text{--}50\%$. Adopting $k_{\text{dust}} = 50\%$, Eq. 8 leads to a distance estimate of $D \approx 3$ pkpc between galaxies *B1/B2* and the observed Ly α intensity peak of $7.5 \times 10^{-18} \text{ erg s}^{-1} \text{ cm}^{-2} \text{ arcsec}^{-2}$ (the $8\text{-}\sigma$ contour in Figure 8). At $\text{SB}_{\text{Ly}\alpha} = 2.8 \times 10^{-18} \text{ erg s}^{-1} \text{ cm}^{-2} \text{ arcsec}^{-2}$ (the $3\text{-}\sigma$ contour in Figure 8), we estimate a distance of ≈ 5 pkpc, which agrees well with the observed extent of the nebula.

The above exercise shows that resonant scattering of Ly α photons produced in nearby star-forming regions may be sufficient for explaining the observed Ly α signals in both systems without invoking additional emission sources. This is in contrast to the recombination radiation scenario discussed in §6.1. It shows that even at 100% escape fraction of ionizing photons, recombination is insufficient for explaining the observed Ly α flux in System *B* and that it would require an escape fraction of $\sim 10\%$ from *A1* for recombination to contribute significantly to the emission signal.

6.3 Systematics in interpreting the spatial and spectral profiles of the nebulae

Due to the clumpy nature of line-emitting gas, the surface brightness profile of extended nebulae is subject to the spatial variation of lensing magnification and its associated uncertainties in the image plane. In principle, gravitational lensing conserves surface brightness of a light-emitting

source. However, the conservation of surface brightness does not apply when the lensed image of the source is not resolved in the data. In our study, the spatial resolution is limited by the size of the seeing disk in ground-based observations. We see that the source-plane image reconstructed from less magnified regions appear to be fainter (e.g., image *a* of System *A*) than those reconstructed from more highly magnified images (e.g., images *b* and *c* of System *A*). This surface brightness discrepancy suggests that the individual clumps, even after being magnified by the cluster lens, are still not resolved by the data. Apart from the decrease of surface brightness in image *a* of System *A* as discussed in §5.1, we also see discrepancy of Ly α surface brightness near critical curves where the magnification factor is much larger (e.g., in System *B*, the Ly α emitting region that straddles the critical curve between images *a* and *b* shows the highest apparent surface brightness across the whole lensed arc). Adopting $\mu \approx 20$ as the fiducial magnification factor near the critical curves, we estimate that the clump size should be $\lesssim 1.5$ kpc in order for the gas clumps to remain unresolved in lensed images recorded under $1''$ seeing. This upper limit is in agreement with clump sizes of cold gas in the CGM constrained in absorption studies (e.g. Zahedy et al. 2019). Furthermore, small-scale substructures in the lens can also introduce additional perturbations to the lensing effect across an extended source (e.g., the unusually large magnification at the location of image *B1e*, see §4.1). In order to accurately quantify the intrinsic surface brightness distribution of extended and clumpy sources in strong lensing fields, a better understanding of the systematic uncertainties of lensing magnification as a function of image position is necessary.

Systematic uncertainties also remain in the shell model analysis on the Ly α line profiles and the interpretation of the velocity gradient derived from spatially-varying Ly α lines in both Systems *A* and *B*. For example, our shell model does not include radiative transfer effects inside the galaxies, which would re-shape the input Ly α line from a single Gaussian into a double-peak profile. This provides a likely explanation for the large redshift observed at the location of the continuum regions in System *A* (see Figure 11). However, a clumpy ISM may also be transparent to Ly α photons, resulting in a wider Gaussian linewidth instead. In addition, because the signal strength is dominated by the much stronger red peak in the Ly α line (see Figure 10), the inferred velocity offset could simply represent a shift in the location of the red peak. The observed blueshifted velocity with increasing projected distance in System *A* (see Figure 11) may also be explained in part due to line-of-sight projection of a uniformly expanding sphere. While a complete 3D radiative transfer model to consider different possible cloud geometry is beyond the scope of this paper, an initial exercise that explores different cloud geometry and velocity field shows that the emergent spectrum will be increasingly blueshifted (redshifted) from the center to the edge of the cloud with decelerating (accelerating) gas expansions. We show one example of such exercise in Appendix D, where we extract the emergent Ly α line profile as a function of projected distance from the center of a spherical cloud that is undergoing expansion with an accelerating or decelerating velocity field. We therefore argue that System *A* is likely

decelerating while System *B* is accelerating as the gas move outward from the star-forming regions.

In summary, the observed Ly α emission morphology in System *A* clearly indicates a more complicated gas geometry than what is assumed in current radiative transfer simulations. In addition, significant uncertainties remain in terms of the origin and the spatial distribution of Ly α emission sources, the effect of local ISM on the Ly α spectra emergent from the star-forming regions prior to the scattering of large-scale gas in the CGM, as well as the effect of dust and gas clumpiness. All of these factors can alter the shape of the emerging line profile, the surface brightness profile, and the velocity gradient of Ly α emission in an extended gas cloud. A more sophisticated radiative transfer model is needed to fully explore the parameter space.

7 SUMMARY AND CONCLUSIONS

Combining the strong cluster lensing power with deep wide-field integral field spectroscopic data, we have carried out a detailed analysis of two giant Ly α arcs to spatially and spectrally resolve gas flows around two active star-forming regions at $z > 3$. Both Ly α nebulae are found to be spatially offset from the associated star-forming region and both exhibit a double-peak profile with a significantly enhanced red peak that indicates expansion/outflowing motions. One of the arcs with Ly α surface brightness of $3.7 \times 10^{-18} \text{ erg s}^{-1} \text{ cm}^{-2} \text{ arcsec}^{-2}$, detected at the $3\text{-}\sigma$ level of significance, stretches over $1'$ around the Einstein radius of the cluster, resolving the velocity field of the line-emitting gas on sub-kpc scales around a group of three star-forming galaxies of $0.3\text{-}1.6 L_*$ at $z = 3.038$. Based on a lens model constructed from deep *HST* images, the de-magnified source-plane Ly α image exhibits a symmetric double-lobe structure of ≈ 30 pkpc across, encompassing the galaxy group. The total integrated Ly α flux across the nebula is $(6.5 \pm 0.1) \times 10^{-17} \text{ erg s}^{-1} \text{ cm}^{-2}$ after correcting lensing magnifications, corresponding to a total Ly α luminosity of $L_{\text{Ly}\alpha} = (5.2 \pm 0.1) \times 10^{42} \text{ erg s}^{-1}$ at $z \approx 3.038$. The second arc with Ly α surface brightness of $2.8 \times 10^{-18} \text{ erg s}^{-1} \text{ cm}^{-2} \text{ arcsec}^{-2}$ ($3\text{-}\sigma$) spans $15''$ in size, roughly centered around a pair of low-mass dwarf Ly α emitters of $\approx 0.03 L_*$ at $z = 3.754$. The total integrated Ly α flux is $(7.4 \pm 0.2) \times 10^{-18} \text{ erg s}^{-1} \text{ cm}^{-2}$, corresponding to a total luminosity of $L_{\text{Ly}\alpha} = (9.8 \pm 0.2) \times 10^{41} \text{ erg s}^{-1}$ at $z \approx 3.754$. Here we summarize the main findings of our study:

(1) A strong variation in the observed Ly α surface brightness is clearly seen across both nebulae, suggesting large spatial fluctuations in the underlying gas properties. While the nebulae at $z = 3.038$ is split into northern and southern lobes bracketing the group of luminous star-forming galaxies, the one at $z = 3.754$ appears to be more symmetrically distributed around the associated low-mass galaxies.

(2) Spatial variations in the kinematics profile of the Ly α emission line are also detected in both nebulae, revealing highly organized velocity fields across the nebulae. We show that such spatial variations, if unaccounted for in integrated Ly α profiles, may lead to biased results in constraining the underlying gas kinematics. By applying a simple expanding shell model to the spatially-varying

$\text{Ly}\alpha$ line, we infer a large velocity gradient of $|\Delta v/\Delta r_{\perp}| \approx 22 - 27 \text{ km s}^{-1} \text{ pkpc}^{-1}$ and high neutral hydrogen column density of $\log N(\text{H I})/\text{cm}^{-2} \gtrsim 19.5$ for both nebulae. The result supports a scenario in which high column density gas is driven outward from the galaxies to beyond 10 pkpc in projected distance into the low-density surroundings.

(3) Combining known star formation properties of the galaxies and the observed extent and surface brightness of the $\text{Ly}\alpha$ signals, we show that the observed $\text{Ly}\alpha$ photons likely originate from a combination of resonant scattering of $\text{Ly}\alpha$ photons from the nearby star-forming regions and recombination radiation due to escaping ionizing photons, although the relative contribution of these two mechanisms cannot be accurately determined with the current data.

Both nebulae provide clear-cut examples of gas outflows that are thought to be widespread at high redshift and may be responsible for metal enrichment of the $\text{Ly}\alpha$ forest in general. While the hydrogen $\text{Ly}\alpha$ line, being the strongest emission line in diffuse, photo-ionized gas, enables sensitive studies of spatially extended outflows beyond active star-forming regions, large uncertainties remain due to the resonant nature of this transition. Future observations targeting non-resonant transitions, such as $[\text{O II}]\lambda\lambda 3727, 3730$, $\text{H}\beta\lambda 4863$, $[\text{O III}]\lambda 5008$, and $\text{H}\alpha\lambda 6565$, within the line-emitting nebulae will provide the necessary discriminating power to resolve the degeneracy between different physical parameters. Based on the observed $\text{Ly}\alpha$ surface brightness in Systems *A* and *B* and under the assumption that the $\text{Ly}\alpha$ emission arises from recombination radiation of photo-ionized gas, we estimate the expected $\text{H}\alpha$ and $\text{H}\beta$ surface brightness to be approximately 3 and $1 \times 10^{-19} \text{ erg s}^{-1} \text{ cm}^{-2} \text{ arcsec}^{-2}$, respectively. The $[\text{O III}]\lambda 5008$ line is expected to be between 3 and 10 times brighter than $\text{H}\beta$ in photo-ionized, low-metallicity gas (e.g. Kewley et al. 2019). While the $\text{H}\alpha$ line is redshifted out of the detection window with existing near-infrared spectrographs on the ground, it is possible to detect $\text{H}\beta\lambda 4863$ and $[\text{O III}]\lambda 5008$ lines in under ≈ 20 hours, within the reach of current observing facilities. We therefore argue that follow-up near-infrared integral field observations, targeting rest-frame optical, non-resonant lines in known $\text{Ly}\alpha$ nebulae, will greatly improve the physical constraints of gas flows around distant star-forming galaxies.

ACKNOWLEDGEMENTS

We thank Erin Boettcher, Fakhri Zahedy, Claude-André Faucher-Giguère and Irina Zhuravleva for helpful discussions. We also thank an anonymous referee for constructive comments that helped improve this paper. HWC and MCC acknowledge partial support from HST-GO-15163.001A and NSF AST-1715692 grants. MG was supported by NASA through the NASA Hubble Fellowship grant HST-HF2-51409. This research has made use of the services of the ESO Science Archive Facility and the Astrophysics Data Service (ADS)⁴. The analysis in this work was greatly facilitated by the following python packages: Numpy (Oliphant 2015), Scipy (Virtanen et al. 2020), Astropy (Astropy Collabo-

ration et al. 2013; Price-Whelan et al. 2018), Matplotlib (Hunter 2007), and MPDAF (Bacon et al. 2016).

DATA AVAILABILITY

The data used in this article are available for download through the Mikulski Archive for Space Telescopes (MAST) and the ESO Science Archive Facility.

REFERENCES

- Adelberger K. L., Steidel C. C., Kollmeier J. A., Reddy N. A., 2006, *ApJ*, **637**, 74
- Arrigoni Battaia F., Hennawi J. F., Prochaska J. X., Oñorbe J., Farina E. P., Cantalupo S., Lusso E., 2019, *MNRAS*, **482**, 3162
- Astropy Collaboration et al., 2013, *A&A*, **558**, A33
- Bacon R., et al., 2010, in Proc. SPIE. p. 773508, doi:10.1117/12.856027
- Bacon R., Piqueras L., Conseil S., Richard J., Shepherd M., 2016, MPDAF: MUSE Python Data Analysis Framework (ascl:1611.003)
- Becker G. D., Rauch M., Sargent W. L. W., 2007, *ApJ*, **662**, 72
- Berg D. A., Erb D. K., Auger M. W., Pettini M., Brammer G. B., 2018, *ApJ*, **859**, 164
- Bertin E., Arnouts S., 1996, *A&AS*, **117**, 393
- Biviano A., et al., 2013, *A&A*, **558**, A1
- Böhringer H., et al., 2001, *A&A*, **369**, 826
- Bordoloi R., Rigby J. R., Tumlinson J., Bayliss M. B., Sharon K., Gladders M. G., Wuyts E., 2016, *MNRAS*, **458**, 1891
- Borisova E., et al., 2016, *ApJ*, **831**, 39
- Bouwens R. J., Illingworth G. D., Franx M., Ford H., 2007, *ApJ*, **670**, 928
- Brinchmann J., Pettini M., Charlot S., 2008, *MNRAS*, **385**, 769
- Bruzual G., Charlot S., 2003, *MNRAS*, **344**, 1000
- Cabanac R. A., Valls-Gabaud D., Lidman C., 2008, *MNRAS*, **386**, 2065
- Cai Z., et al., 2017, *ApJ*, **837**, 71
- Cai Z., et al., 2019, *ApJS*, **245**, 23
- Calzetti D., Armus L., Bohlin R. C., Kinney A. L., Koornneef J., Storchi-Bergmann T., 2000, *ApJ*, **533**, 682
- Caminha G. B., et al., 2016a, *A&A*, **587**, A80
- Caminha G. B., et al., 2016b, *A&A*, **595**, A100
- Caminha G. B., et al., 2017, *A&A*, **607**, A93
- Cantalupo S., 2017, in Fox A., Davé R., eds, *Astrophysics and Space Science Library Vol. 430, Gas Accretion onto Galaxies*. p. 195 (arXiv:1612.00491), doi:10.1007/978-3-319-52512-9_9
- Cantalupo S., Porciani C., Lilly S. J., Miniati F., 2005, *ApJ*, **628**, 61
- Cantalupo S., Lilly S. J., Haehnelt M. G., 2012, *MNRAS*, **425**, 1992
- Cantalupo S., Arrigoni-Battaia F., Prochaska J. X., Hennawi J. F., Madau P., 2014, *Nature*, **506**, 63
- Cantalupo S., et al., 2019, *MNRAS*, **483**, 5188
- Carnall A. C., McLure R. J., Dunlop J. S., Davé R., 2018, *MNRAS*, **480**, 4379
- Chen H.-W., 2017, *Outskirts of Distant Galaxies in Absorption*. p. 291, doi:10.1007/978-3-319-56570-5_9
- Chen H.-W., Prochaska J. X., Gnedin N. Y., 2007, *ApJ*, **667**, L125
- Chen H.-W., Gauthier J.-R., Sharon K., Johnson S. D., Nair P., Liang C. J., 2014, *MNRAS*, **438**, 1435
- Claeysens A., et al., 2019, *MNRAS*, **489**, 5022
- Coe D., et al., 2013, *ApJ*, **762**, 32
- Conroy C., 2013, *ARA&A*, **51**, 393
- Conroy C., Gunn J. E., 2010, *ApJ*, **712**, 833

⁴ <https://ui.adsabs.harvard.edu/classic-form>

- Conroy C., Gunn J. E., White M., 2009, *ApJ*, **699**, 486
- Crowther P. A., 2007, *ARA&A*, **45**, 177
- Dijkstra M., 2014, *Publ. Astron. Soc. Australia*, **31**, e040
- Dijkstra M., 2017, arXiv e-prints, p. [arXiv:1704.03416](https://arxiv.org/abs/1704.03416)
- Dijkstra M., Kramer R., 2012, *MNRAS*, **424**, 1672
- Dijkstra M., Haiman Z., Spaans M., 2006, *ApJ*, **649**, 14
- Draine B. T., 2011, *Physics of the Interstellar and Intergalactic Medium*
- Ebeling H., Edge A. C., Henry J. P., 2001, *ApJ*, **553**, 668
- Ebeling H., Ma C. J., Kneib J. P., Jullo E., Courtney N. J. D., Barrett E., Edge A. C., Le Borgne J. F., 2009, *MNRAS*, **395**, 1213
- Eichner T., et al., 2013, *ApJ*, **774**, 124
- Eldridge J. J., Stanway E. R., Xiao L., McClelland L. A. S., Taylor G., Ng M., Greis S. M. L., Bray J. C., 2017, *Publ. Astron. Soc. Australia*, **34**, e058
- Elíasdóttir Á., et al., 2007, preprint, ([arXiv:0710.5636](https://arxiv.org/abs/0710.5636))
- Erb D. K., Steidel C. C., Shapley A. E., Pettini M., Reddy N. A., Adelberger K. L., 2006, *ApJ*, **646**, 107
- Erb D. K., et al., 2014, *ApJ*, **795**, 33
- Erb D. K., Steidel C. C., Chen Y., 2018, *ApJ*, **862**, L10
- Erb D. K., Berg D. A., Auger M. W., Kaplan D. L., Brammer G., Pettini M., 2019, *ApJ*, **884**, 7
- Faucher-Giguère C.-A., Kereš D., Dijkstra M., Hernquist L., Zaldarriaga M., 2010, *ApJ*, **725**, 633
- Feltre A., Charlot S., Gutkin J., 2016, *MNRAS*, **456**, 3354
- Feltre A., et al., 2020, arXiv e-prints, p. [arXiv:2007.01878](https://arxiv.org/abs/2007.01878)
- Ferland G. J., et al., 2017, *Rev. Mex. Astron. Astrofis.*, **53**, 385
- Florian M. K., et al., 2020, arXiv e-prints, p. [arXiv:2006.11387](https://arxiv.org/abs/2006.11387)
- Franx M., Illingworth G. D., Kelson D. D., van Dokkum P. G., Tran K.-V., 1997, *ApJ*, **486**, L75
- Frye B., Broadhurst T., 1998, *ApJ*, **499**, L115
- Frye B., Broadhurst T., Benítez N., 2002, *ApJ*, **568**, 558
- Gould A., Weinberg D. H., 1996, *ApJ*, **468**, 462
- Grazian A., et al., 2017, *A&A*, **602**, A18
- Gronke M., 2017, *A&A*, **608**, A139
- Gronke M., Dijkstra M., 2014, *MNRAS*, **444**, 1095
- Gronke M., Bull P., Dijkstra M., 2015, *ApJ*, **812**, 123
- Gronke M., Dijkstra M., McCourt M., Oh S. P., 2016, *ApJ*, **833**, L26
- Gutkin J., Charlot S., Bruzual G., 2016, *MNRAS*, **462**, 1757
- Hansen M., Oh S. P., 2006, *MNRAS*, **367**, 979
- Hayes M., 2015, *Publ. Astron. Soc. Australia*, **32**, e027
- Heckman T. M., Alexandroff R. M., Borthakur S., Overzier R., Leitherer C., 2015, *ApJ*, **809**, 147
- Hennawi J. F., Prochaska J. X., 2013, *ApJ*, **766**, 58
- Hennawi J. F., Prochaska J. X., Kollmeier J., Zheng Z., 2009, *ApJ*, **693**, L49
- Hezaveh Y. D., et al., 2016, *ApJ*, **823**, 37
- Hoag A., et al., 2019, *MNRAS*, **488**, 706
- Hogan C. J., Weymann R. J., 1987, *MNRAS*, **225**, 1P
- Hunter J. D., 2007, *Computing in Science and Engineering*, **9**, 90
- Johnson S. D., Chen H.-W., Mulchaey J. S., Tripp T. M., Prochaska J. X., Werk J. K., 2014, *MNRAS*, **438**, 3039
- Johnson T. L., et al., 2017, *ApJ*, **843**, L21
- Jullo E., Kneib J.-P., Limousin M., Elíasdóttir Á., Marshall P. J., Verdugo T., 2007, *New Journal of Physics*, **9**, 447
- Kassiola A., Kovner I., 1993, *ApJ*, **417**, 450
- Kehrig C., Vílchez J. M., Guerrero M. A., Iglesias-Páramo J., Hunt L. K., Duarte-Puertas S., Ramos-Larios G., 2018, *MNRAS*, **480**, 1081
- Kelly P. L., et al., 2018, *Nature Astronomy*, **2**, 334
- Kennicutt R. C., Evans N. J., 2012, *ARA&A*, **50**, 531
- Kewley L. J., Nicholls D. C., Sutherland R. S., 2019, *ARA&A*, **57**, 511
- Kollmeier J. A., Zheng Z., Davé R., Gould A., Katz N., Miralda-Escudé J., Weinberg D. H., 2010, *ApJ*, **708**, 1048
- Kulas K. R., Shapley A. E., Kollmeier J. A., Zheng Z., Steidel C. C., Hainline K. N., 2012, *ApJ*, **745**, 33
- Lam D., Broadhurst T., Diego J. M., Lim J., Coe D., Ford H. C., Zheng W., 2014, *ApJ*, **797**, 98
- Laursen P., Sommer-Larsen J., Andersen A. C., 2009, *ApJ*, **704**, 1640
- Leclercq F., et al., 2017, *A&A*, **608**, A8
- Leclercq F., et al., 2020, *A&A*, **635**, A82
- Leitherer C., et al., 1999, *ApJS*, **123**, 3
- Lemaux B. C., et al., 2020, arXiv e-prints, p. [arXiv:2007.01310](https://arxiv.org/abs/2007.01310)
- Livermore R. C., et al., 2012, *MNRAS*, **427**, 688
- Lopez S., et al., 2018, *Nature*, **554**, 493
- Ma X., Hopkins P. F., Faucher-Giguère C.-A., Zolman N., Muratov A. L., Kereš D., Quataert E., 2016, *MNRAS*, **456**, 2140
- Madau P., Dickinson M., 2014, *ARA&A*, **52**, 415
- Martin C. L., Shapley A. E., Coil A. L., Kornei K. A., Bundy K., Weiner B. J., Noeske K. G., Schiminovich D., 2012, *ApJ*, **760**, 127
- Maseda M. V., et al., 2017, *A&A*, **608**, A4
- Matthee J., Sobral D., Gronke M., Paulino-Afonso A., Stefanon M., Röttgering H., 2018, *A&A*, **619**, A136
- McKean J. P., et al., 2007, *MNRAS*, **378**, 109
- Molino A., et al., 2017, *MNRAS*, **470**, 95
- Morrissey P., et al., 2018, *ApJ*, **864**, 93
- Mortensen K., Keerthi Vasani G. C., Jones T., Faucher-Giguère C.-A., Sanders R., Ellis R. S., Leethochawalit N., Stark D. P., 2020, arXiv e-prints, p. [arXiv:2006.00006](https://arxiv.org/abs/2006.00006)
- Nanayakkara T., et al., 2019, *A&A*, **624**, A89
- Neufeld D. A., 1991, *ApJ*, **370**, L85
- Oliphant T. E., 2015, *Guide to NumPy*, 2nd edn. CreateSpace Independent Publishing Platform, USA
- Orlitová I., Verhamme A., Henry A., Scarlata C., Jaskot A., Oey M. S., Schaerer D., 2018, *A&A*, **616**, A60
- Osterbrock D. E., Ferland G. J., 2006, *Astrophysics of gaseous nebulae and active galactic nuclei*
- Patrício V., et al., 2016, *MNRAS*, **456**, 4191
- Pettini M., Steidel C. C., Adelberger K. L., Dickinson M., Gialalisco M., 2000, *ApJ*, **528**, 96
- Postman M., et al., 2012, *ApJS*, **199**, 25
- Price-Whelan A. M., et al., 2018, *AJ*, **156**, 123
- Rauch M., Sargent W. L. W., Barlow T. A., Simcoe R. A., 2002, *ApJ*, **576**, 45
- Rauch M., et al., 2008, *ApJ*, **681**, 856
- Rauch M., Becker G. D., Haehnelt M. G., Gauthier J.-R., Ravindranath S., Sargent W. L. W., 2011, *MNRAS*, **418**, 1115
- Rauch M., Becker G. D., Haehnelt M. G., Gauthier J.-R., Sargent W. L. W., 2013, *MNRAS*, **429**, 429
- Rauch M., Becker G. D., Haehnelt M. G., 2016, *MNRAS*, **455**, 3991
- Reddy N. A., Steidel C. C., Pettini M., Adelberger K. L., Shapley A. E., Erb D. K., Dickinson M., 2008, *ApJS*, **175**, 48
- Reddy N. A., Pettini M., Steidel C. C., Shapley A. E., Erb D. K., Law D. R., 2012, *ApJ*, **754**, 25
- Ribeiro B., et al., 2020, arXiv e-prints, p. [arXiv:2007.01322](https://arxiv.org/abs/2007.01322)
- Richard J., et al., 2020, arXiv e-prints, p. [arXiv:2009.09784](https://arxiv.org/abs/2009.09784)
- Rosati P., et al., 2014, *The Messenger*, **158**, 48
- Rubin K. H. R., et al., 2018, *ApJ*, **859**, 146
- Rudie G. C., Steidel C. C., Pettini M., Trainor R. F., Strom A. L., Hummels C. B., Reddy N. A., Shapley A. E., 2019, *ApJ*, **885**, 61
- Schaerer D., Vacca W. D., 1998, *ApJ*, **497**, 618
- Schaerer D., Hayes M., Verhamme A., Teyssier R., 2011, *A&A*, **531**, A12
- Schlafly E. F., Finkbeiner D. P., 2011, *ApJ*, **737**, 103
- Shapley A. E., 2011, *ARA&A*, **49**, 525
- Shapley A. E., Steidel C. C., Pettini M., Adelberger K. L., 2003, *ApJ*, **588**, 65

Shibuya T., Ouchi M., Nakajima K., Yuma S., Hashimoto T., Shimasaku K., Mori M., Umemura M., 2014, *ApJ*, **785**, 64

Steidel C. C., Bogosavljević M., Shapley A. E., Kollmeier J. A., Reddy N. A., Erb D. K., Pettini M., 2011, *ApJ*, **736**, 160

Swinbank A. M., Bower R. G., Smith G. P., Wilman R. J., Smail I., Ellis R. S., Morris S. L., Kneib J. P., 2007, *MNRAS*, **376**, 479

Trainor R. F., Steidel C. C., 2012, *ApJ*, **752**, 39

Tumlinson J., Peebles M. S., Werk J. K., 2017, *ARA&A*, **55**, 389

Umetsu K., et al., 2012, *ApJ*, **755**, 56

Vanzella E., et al., 2010, *ApJ*, **725**, 1011

Vanzella E., et al., 2017, *MNRAS*, **465**, 3803

Verhamme A., Schaerer D., Maselli A., 2006, *A&A*, **460**, 397

Verhamme A., Schaerer D., Atek H., Tapken C., 2008, *A&A*, **491**, 89

Virtanen P., et al., 2020, *Nature Methods*, **17**, 261

Voges W., et al., 1999, *A&A*, **349**, 389

Wisotzki L., et al., 2016, *A&A*, **587**, A98

Wisotzki L., et al., 2018, *Nature*, **562**, 229

Xue R., et al., 2017, *ApJ*, **837**, 172

Yang H., et al., 2017, *ApJ*, **844**, 171

Zahedy F. S., Chen H.-W., Rauch M., Wilson M. L., Zabludoff A., 2016, *MNRAS*, **458**, 2423

Zahedy F. S., Chen H.-W., Johnson S. D., Pierce R. M., Rauch M., Huang Y.-H., Weiner B. J., Gauthier J.-R., 2019, *MNRAS*, **484**, 2257

Zitrin A., et al., 2012, *ApJ*, **749**, 97

APPENDIX A: LENS CONSTRAINTS AND PARAMETERS

In Table A1, we list the coordinates of all multiple images used as constraints in our lens modeling process, while the best-fit parameters for the fiducial and fine-tuned model are listed in Tables A2 and A3, respectively.

APPENDIX B: PHOTOMETRY FOR INDIVIDUAL IMAGES OF SYSTEMS *A* AND *B*

In §4.1, we presented the photometric magnitudes of galaxies in Systems *A* and *B* after correcting the lensing magnification and averaging among multiple images. Here in Table B1, we list the direct measurements from the data for each individual images without correcting for lensing effect. Note that the Galactic extinction is corrected for each bandpass.

Table A1. Coordinates and redshifts of multiple images included for lens modeling.

Image ID	RA	DEC	Redshift
<i>A2a</i>	181.562648	-8.796683	3.0378
<i>A2b</i>	181.562497	-8.804908	3.0378
<i>A2c</i>	181.560573	-8.808988	3.0378
<i>A31a</i>	181.562535	-8.796884	3.0384
<i>A31b</i>	181.562501	-8.804524	3.0384
<i>A31c</i>	181.560104	-8.809551	3.0384
<i>A32a</i>	181.562551	-8.796809	3.0384
<i>A32b</i>	181.562492	-8.804617	3.0384
<i>A32c</i>	181.560204	-8.809411	3.0384
<i>B1a</i>	181.566558	-8.804480	3.7540
<i>B1b</i>	181.566475	-8.804733	3.7540
<i>B1c</i>	181.566475	-8.805147	3.7540
<i>B1d</i>	181.566275	-8.806328	3.7540
<i>B1e</i>	181.565591	-8.807690	3.7540
<i>B2a</i>	181.566605	-8.804400	3.7540
<i>B2c</i>	181.566494	-8.805077	3.7540
<i>B2d</i>	181.566250	-8.806446	3.7540
<i>B2e</i>	181.565675	-8.807566	3.7540
<i>1a</i>	181.550916	-8.797422	1.0121
<i>1b</i>	181.549604	-8.799294	1.0121
<i>1c</i>	181.548870	-8.806655	1.0121
<i>3a</i>	181.550570	-8.795568	1.0433
<i>3b</i>	181.547611	-8.799811	1.0433
<i>3c</i>	181.548607	-8.805281	1.0433
<i>4a</i>	181.552987	-8.794699	1.4248
<i>4b</i>	181.548830	-8.800057	1.4248
<i>4c</i>	181.549752	-8.807965	1.4248
<i>5a</i>	181.553557	-8.795189	1.4254
<i>5b</i>	181.554237	-8.801552	1.4254
<i>5c</i>	181.550005	-8.808098	1.4254
<i>6a</i>	181.549979	-8.796362	1.4255
<i>6b</i>	181.548139	-8.797058	1.4255
<i>6c</i>	181.548050	-8.809283	1.4255
<i>8a</i>	181.553657	-8.795756	1.4864
<i>8b</i>	181.554524	-8.801104	1.4864
<i>8c</i>	181.549957	-8.808887	1.4864
<i>9a</i>	181.546741	-8.793144	1.9600
<i>9b</i>	181.543273	-8.797812	1.9600
<i>9c</i>	181.544378	-8.807486	1.9600
<i>10a</i>	181.552450	-8.795001	2.5393
<i>10b</i>	181.546604	-8.797465	2.5393
<i>10c</i>	181.550487	-8.799957	2.5393
<i>10d</i>	181.554894	-8.800160	2.5393
<i>10e</i>	181.548827	-8.811813	2.5393
<i>12a</i>	181.548632	-8.793717	3.3890
<i>12b</i>	181.546121	-8.795387	3.3890
<i>12c</i>	181.553268	-8.800197	3.3890

We adopt the multiple image identifications from Caminha et al. (2017), while excluding image systems 2, 7, 13, 21, 24 and 27 (see §3 for detailed discussions). We rename their image system 11 to be *A2*, and add *A31* and *A32* (the north and south substructures of *A3*). Similarly, we rename image system 14 to be *B1*, and add *B2* (the fainter structure near *B1* at the same redshift). We also update redshifts for *A2*, *A3*, *B1* and *B2* to be their best-fit values from fitting the observed emission lines (see §4). For the fiducial model, we use all images listed except for *A31*, *A32* and *B2*. For the fine-tuned model, we only use systems *A2*, *A31*, *A32*, *B1* and *B2*, excluding all other lensed systems, in order to optimise the model specifically for *A* and *B*.

Table A1 – *continued*

Image ID	RA	DEC	Redshift
15a	181.555962	-8.791635	3.7611
15b	181.557600	-8.803056	3.7611
15c	181.551748	-8.810964	3.7611
16a	181.554584	-8.791202	3.7617
16b	181.546465	-8.799671	3.7617
16c	181.556520	-8.802471	3.7617
17a	181.556136	-8.795620	3.8224
17b	181.556958	-8.799422	3.8224
18a	181.555376	-8.796714	4.0400
18b	181.555927	-8.798595	4.0400
19a	181.562084	-8.794875	4.0520
19b	181.561873	-8.805239	4.0520
19c	181.559788	-8.809463	4.0520
20a	181.547472	-8.800476	4.0553
20b	181.556839	-8.803813	4.0553
22a	181.544328	-8.791418	4.2913
22b	181.540282	-8.796562	4.2913
22c	181.540884	-8.806094	4.2913
23a	181.563252	-8.796893	4.7293
23b	181.563537	-8.803670	4.7293
23c	181.559832	-8.811526	4.7293
25a	181.559714	-8.796562	5.7927
25b	181.560102	-8.800177	5.7927
26a	181.550711	-8.803112	6.0106
26b	181.551211	-8.803668	6.0106

Table A2. Best-fit *LENSTOOL* parameters of the fiducial lens model.

First cluster-scale PIEMD halo	
x (")	$-1.420^{+0.314}_{-0.157}$
y (")	$1.047^{+0.149}_{-0.109}$
ϵ	$0.598^{+0.036}_{-0.005}$
θ (deg)	$19.790^{+1.265}_{-0.268}$
r_c (kpc)	$35.941^{+0.814}_{-1.984}$
σ_v (km/s)	$986.284^{+14.338}_{-8.487}$
Second cluster-scale PIEMD halo	
x (")	$-11.592^{+0.347}_{-0.291}$
y (")	$5.729^{+0.001}_{-2.367}$
ϵ	$0.429^{+0.076}_{-0.0}$
θ (deg)	$100.850^{+3.853}_{-1.232}$
r_c (kpc)	$212.843^{+9.732}_{-28.724}$
σ_v (km/s)	$1078.762^{+5.161}_{-63.885}$
Third cluster-scale PIEMD halo	
x (")	$29.401^{+0.629}_{-0.437}$
y (")	$-8.171^{+0.710}_{-0.239}$
ϵ	$0.453^{+0.009}_{-0.074}$
θ (deg)	$8.895^{+3.891}_{-2.322}$
r_c (kpc)	$88.386^{+5.336}_{-6.934}$
σ_v (km/s)	$746.233^{+31.612}_{-18.050}$
External Shear	
γ_{shear}	$0.334^{+0.031}_{-0.022}$
θ_{shear} (deg)	$92.177^{+1.939}_{-1.357}$
Galaxy members	
$r_{g,t}^0$ (kpc)	$22.940^{+2.600}_{-2.840}$
$\sigma_{g,v}^0$ (km/s)	$197.907^{+14.636}_{-11.880}$

Positions x and y are relative to the position of the BCG at RA = 181.550648° and DEC = -8.800952°, with positive offsets point to west and north.

Table A3. Best-fit *LENSTOOL* parameters of the fine-tuned lens model.

Third cluster-scale PIEMD halo	
x (")	$13.847^{+0.497}_{-9.301}$
y (")	$-5.008^{+0.063}_{-1.849}$
ϵ	$0.573^{+0.102}_{-0.098}$
θ (deg)	$9.202^{+1.418}_{-1.431}$
r_c (kpc)	$97.114^{+3.834}_{-11.217}$
σ_v (km/s)	$799.654^{+8.018}_{-43.115}$
Gm1 PIEMD halo	
$r_{g,t}$ (kpc)	$28.104^{+22.0}_{-20.0}$
$\sigma_{g,v}$ (km/s)	$203.412^{+68.500}_{-63.907}$
Gm2 PIEMD halo	
$r_{g,t}$ (kpc)	$24.369^{+26.0}_{-20.0}$
$\sigma_{g,v}$ (km/s)	$210.705^{+61.428}_{-52.603}$
Gm3 PIEMD halo	
$r_{g,t}$ (kpc)	$7.272^{+12.8}_{-6.0}$
$\sigma_{g,v}$ (km/s)	$83.873^{+28.112}_{-23.457}$

Positions x and y are relative to the position of the BCG at $RA = 181.550648^\circ$ and $DEC = -8.800952^\circ$, with positive offsets point to west and north. The first and second cluster-scale PIEMD halos, external shear, and galaxy members are fixed to their best-fit values from the fiducial model, as listed in Table A2.

Table B1. Photometry from *HST* data, directly measured for each individual image without correcting for lensing magnification. The foreground Galactic extinction is corrected (see §4.1 for details).

	F330W ^a	F390W	F435W	F475W	F606W	F625W	F775W	F814W
<i>A1</i>	> 23.94	24.16 ± 0.08	23.35 ± 0.03	22.94 ± 0.02	22.42 ± 0.07	22.31 ± 0.01	22.21 ± 0.01	22.22 ± 0.01
<i>A2a</i>	> 26.07	25.18 ± 0.13	24.57 ± 0.05	24.33 ± 0.03	24.05 ± 0.03	23.77 ± 0.02	23.72 ± 0.03	23.70 ± 0.01
<i>A2b</i>	> 26.80	24.87 ± 0.09	24.22 ± 0.05	24.07 ± 0.03	23.53 ± 0.02	23.31 ± 0.02	23.19 ± 0.02	23.17 ± 0.01
<i>A2c</i>	> 27.26	24.51 ± 0.32	23.78 ± 0.04	23.69 ± 0.03	23.22 ± 0.02	23.04 ± 0.02	23.04 ± 0.02	22.98 ± 0.01
<i>A3a</i>	> 26.59	25.98 ± 0.21	25.04 ± 0.07	24.67 ± 0.05	24.24 ± 0.08	24.09 ± 0.03	24.08 ± 0.03	24.05 ± 0.02
<i>A3b</i>	> 27.85	25.45 ± 0.15	25.03 ± 0.10	24.52 ± 0.05	23.83 ± 0.02	23.70 ± 0.03	23.51 ± 0.03	23.43 ± 0.01
<i>A3c</i>	> 26.49	24.99 ± 0.11	24.55 ± 0.08	24.23 ± 0.04	23.67 ± 0.02	23.54 ± 0.03	23.43 ± 0.03	23.39 ± 0.02
	F850LP	F105W	F110W	F125W	F140W	F160W		
<i>A1</i>	22.20 ± 0.02	22.22 ± 0.01	22.20 ± 0.01	22.21 ± 0.01	22.03 ± 0.01	21.86 ± 0.01		
<i>A2a</i>	23.67 ± 0.03	23.82 ± 0.02	23.86 ± 0.02	23.90 ± 0.02	23.73 ± 0.02	23.68 ± 0.02		
<i>A2b</i>	23.21 ± 0.03	23.20 ± 0.01	23.18 ± 0.01	23.21 ± 0.02	23.04 ± 0.01	22.92 ± 0.01		
<i>A2c</i>	23.01 ± 0.03	23.24 ± 0.02	23.26 ± 0.01	23.31 ± 0.02	23.14 ± 0.01	23.12 ± 0.01		
<i>A3a</i>	24.08 ± 0.05	24.16 ± 0.03	24.14 ± 0.02	24.22 ± 0.03	23.96 ± 0.02	23.86 ± 0.02		
<i>A3b</i>	23.29 ± 0.03	23.33 ± 0.01	23.30 ± 0.01	23.26 ± 0.01	23.10 ± 0.01	22.95 ± 0.01		
<i>A3c</i>	23.38 ± 0.03	23.54 ± 0.02	23.54 ± 0.01	23.59 ± 0.02	23.38 ± 0.02	23.15 ± 0.01		
	F450W ^b	F475W	F606W	F625W	F775W	F814W	F850LP	F105W
<i>B1a</i>	> 27.42	27.25 ± 0.32	26.48 ± 0.11	26.38 ± 0.16	25.95 ± 0.13	25.98 ± 0.09	25.82 ± 0.15	26.36 ± 0.13
<i>B1c</i>	> 27.39	27.09 ± 0.27	26.34 ± 0.09	26.07 ± 0.11	25.78 ± 0.11	26.00 ± 0.08	26.23 ± 0.21	26.48 ± 0.14
<i>B1d</i>	> 27.25	27.46 ± 0.41	26.43 ± 0.10	26.17 ± 0.13	26.14 ± 0.15	26.26 ± 0.11	26.15 ± 0.21	26.82 ± 0.19
<i>B1e</i>	> 27.41	26.97 ± 0.25	26.17 ± 0.24	25.73 ± 0.09	25.62 ± 0.09	25.77 ± 0.07	25.63 ± 0.13	25.81 ± 0.09
<i>B2a</i>	> 27.39	> 27.81 ^c	27.04 ± 0.19	26.67 ± 0.21	26.40 ± 0.20	26.23 ± 0.10	26.78 ± 0.37	26.45 ± 0.14
<i>B2c</i>	> 27.37	> 27.82 ^c	26.74 ± 0.13	26.85 ± 0.24	26.37 ± 0.18	26.36 ± 0.12	25.97 ± 0.17	26.25 ± 0.12
<i>B2d</i>	> 27.43	27.69 ± 0.49	27.24 ± 0.22	27.41 ± 0.41	26.18 ± 0.17	26.48 ± 0.13	26.08 ± 0.20	26.97 ± 0.22
<i>B2e</i>	> 27.24	27.62 ± 0.49	27.22 ± 0.20	26.51 ± 0.19	26.93 ± 0.34	26.80 ± 0.18	26.56 ± 0.30	26.74 ± 0.20
	F110W	F125W	F140W	F160W				
<i>B1a</i>	26.41 ± 0.10	26.24 ± 0.13	26.41 ± 0.13	26.69 ± 0.17				
<i>B1c</i>	26.39 ± 0.09	26.44 ± 0.15	26.44 ± 0.13	26.30 ± 0.12				
<i>B1d</i>	26.39 ± 0.09	26.67 ± 0.19	26.77 ± 0.17	26.47 ± 0.14				
<i>B1e</i>	25.74 ± 0.10	25.97 ± 0.10	26.02 ± 0.11	26.26 ± 0.15				
<i>B2a</i>	26.39 ± 0.10	26.49 ± 0.16	26.29 ± 0.11	26.09 ± 0.10				
<i>B2c</i>	26.33 ± 0.09	26.22 ± 0.13	26.19 ± 0.10	26.00 ± 0.09				
<i>B2d</i>	26.84 ± 0.14	26.88 ± 0.23	26.68 ± 0.16	26.66 ± 0.16				
<i>B2e</i>	27.09 ± 0.10	26.36 ± 0.14	26.44 ± 0.15	26.45 ± 0.15				

^a 2σ UV flux upper limit, averaged among the F225W, F275W and F336W bandpasses.^b 2σ UV flux upper limit, averaged among the F225W, F275W, F336W, F390W and F435W bandpasses.^c 2σ flux upper limit.

APPENDIX C: FITTING A SHELL MODEL TO STACKED SPECTRA OBTAINED OVER A LARGE AREA WITH FIXED INTRINSIC $\text{Ly}\alpha$ LINE WIDTH σ_I

In §5.3, we have shown that the best-fit shell models for stacked spectra extracted from a large area in both Systems *A* and *B* require the intrinsic $\text{Ly}\alpha$ line width σ_i to be much larger than the observed nebular emission line width. We argue that the large σ_i is caused by the smearing effect due to the velocity gradient in the nebulae. Here in Figure C1, we show the best-fit models for the same spectra shown in the top row of Figure 10 in the main text, and demonstrate that by fixing σ_i to the observed values from galaxy spectra, the best-fit models provide a worse fit to the data.

APPENDIX D: $\text{Ly}\alpha$ LINE PROFILE FROM ACCELERATING AND DECELERATING EXPANDING CLOUDS

We present the $\text{Ly}\alpha$ line profiles emergent at different distances from the center of a spherical cloud undergoing, respectively, an accelerating and decelerating expansion. The physical parameters of the cloud are $\log N(\text{H I})/\text{cm}^{-2} = 20$, $\sigma_i = 0$ km/s (i.e., all $\text{Ly}\alpha$ photons are emitted at the same frequency), and $T_{\text{eff}} = 10^4$ K. The accelerating cloud has a velocity field changing from 0 km/s at the center to 400 km/s at the outer edge of the cloud with a constant radial acceleration, while the decelerating cloud has a reverse gradient changing from 0 to 400 km/s from the outer edge to the center of the cloud. We extract the emergent $\text{Ly}\alpha$ line profiles in two projected distance bins from the cloud center, with an inner bin corresponding to the distance range $[0, 0.5R_{\text{max}}]$ and an outer bin corresponding to $[0.5R_{\text{max}}, R_{\text{max}}]$, where R_{max} is the radius of the cloud. Note that given a fixed $N(\text{H I})$, changing the physical value of R_{max} does not change the shape of the emergent $\text{Ly}\alpha$ profile and therefore R_{max} is not a parameter in the model.

The $\text{Ly}\alpha$ profiles from these two bins are shown in Figure D1. For the decelerating cloud, the dominant red peak is more blueshifted in the outer bin, while the opposite trend is observed for the accelerating cloud. While the amount of shift in velocity and the profile shapes do not match well with the observed $\text{Ly}\alpha$ profiles presented in this work, this simple exercise demonstrates that differential velocity fields in expanding clouds might be a plausible mechanism to produce velocity gradients seen in spatially-resolved $\text{Ly}\alpha$ profiles.

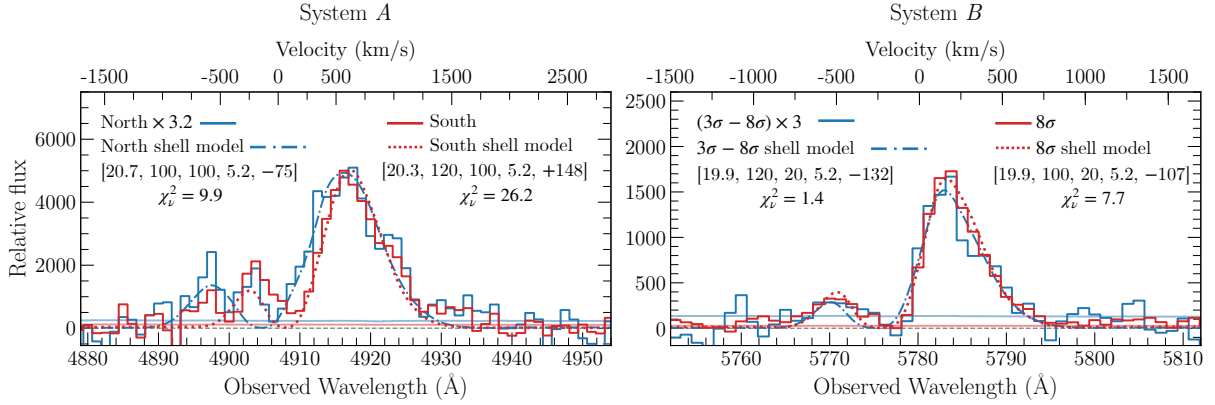


Figure C1. *Left:* Stacked spectra from all spaxels within the $3\text{-}\sigma$ contour in System A, divided into northern and southern nebulae (see Figures 1 and 6). The best-fit models are shown in dash-dotted and dotted curves for the northern and southern nebula, respectively. To obtain the best-fit models, we fix the intrinsic Ly α line width σ_i to be 95 km/s, corresponding to the observed line width measured from the nebular emission lines (see §4.3 and Table 5). Compared with the best-fit models shown in Figure 10 in the main text where σ_i is a free parameter, the models shown here with a fixed σ_i provide a worse fit to the data (particularly on the blue peak), which is also reflected with the increased χ^2_ν . *Right:* Stacked spectral from low- and high-surface brightness regions in System B, extracted from within and outside of the $8\text{-}\sigma$ contours. The best-fit models are shown in dash-dotted and dotted curves for low- and high-surface brightness spectra, respectively. Similar to the models for System A, we fix σ_i to be 20 km/s as measured from the galaxy spectrum. Although these models with fixed σ_i also provide a worse fit to the data compared with the models presented in Figure 10 where σ_i is a free parameter, the difference in χ^2_ν is not as significant as the difference seen in System A. This is consistent with System A having a steeper velocity gradient across the nebulae, leading to a more significant smearing effect in the stacked spectra from a large area.

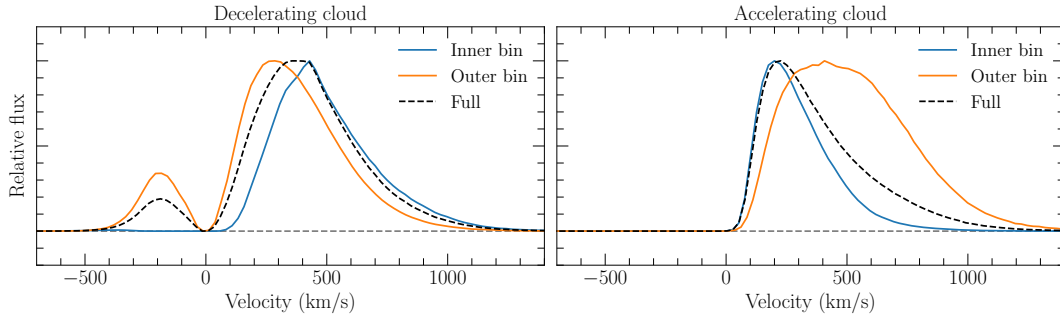


Figure D1. *Left:* Emergent Ly α profiles extracted from the inner and outer bins of a decelerating expanding cloud. The inner and outer bins correspond to the projected distance range of $[0, 0.5R_{\text{max}}]$ and $[0.5R_{\text{max}}, R_{\text{max}}]$ from the center of the cloud, respectively, where R_{max} is the radius of the cloud. The dominant red peak of the Ly α profiles is more blueshifted in the outer bin. The full spectrum extracted from the entire cloud is shown in the dashed black curve. *Right:* same as the left panel but for an accelerating expanding cloud. The profile is more redshifted in the outer bin, contrary to the trend observed for a decelerating cloud.